Applied Energy 206 (2017) 1609–1631

Contents lists available at ScienceDirect

Applied Energy

journal homepage: www.elsevier.com/locate/apenergy

Pitch control for ships with diesel mechanical and hybrid propulsion: Modelling, validation and performance quantification

R.D. Geertsma[a,b,*], R.R. Negenborn[a], K. Visser[a,b], M.A. Loonstijn[a], J.J. Hopman[a]

[a] Department of Maritime & Transport Technology, Delft University of Technology, The Netherlands
[b] Faculty of Military Sciences, Netherlands Defence Academy, The Netherlands

HIGHLIGHTS

- A MVFP propulsion model for comparative ship and control system studies is proposed.
- Fuel consumption, acceleration, thermal loading & propeller cavitation are evaluated.
- Benchmark MOPs quantify these criteria within an hour simulation time.
- The propulsion model is validated with FAT and SAT data from a case study navy ship.
- Control can save 30% fuel, reduce thermal loading by 90 K and acceleration time by 50%.

ARTICLE INFO

Keywords:
Mechanical propulsion
Non-linear control systems
Marine systems
Modelling and simulation
Validation
Power systems

ABSTRACT

Ships, in particular service vessels, need to reduce fuel consumption, emissions and cavitation noise while maintaining manoeuvrability and preventing engine overloading. Diesel mechanical propulsion with controllable pitch propellers can provide high fuel efficiency with good manoeuvrability. However, the conventional control strategy with fixed combinator curves limits control freedom in trading-off performance characteristics. In order to evaluate performance of current state-of-the-art and future alternative propulsion systems and their control, a validated propulsion system model is required. To this end, this paper proposes a propulsion model with a Mean Value First Principle (MVFP) diesel engine model that can be parameterised with publicly available manufacturer data and further calibrated with obligatory FAT measurements. The model uses a novel approach to predict turbocharger performance based on Zinner blowdown, the Büchi power and flow balance and the elliptic law for turbines, and does not require detailed information such as compressor and turbine maps. This model predicts system performance within 5% of actual measurements during Factory Acceptance Tests (FAT) of the diesel engines and Sea Acceptance Tests (SAT) of a case study navy ship. Moreover, this paper proposes measures of performance that objectively quantify the fuel consumption, acceleration rate, engine thermal loading and propeller cavitation during trial, design and off-design conditions in specified benchmark manoeuvres, within an hour simulation time. In our experiments, we find that, depending on the control strategy, up to 30% of fuel can be saved, thermal engine loading can be reduced by 90 K, and acceleration time by 50% for a case study *Holland* class patrol vessel.

1. Introduction

The green house gas reduction targets set during the United Nations climate change conference 2015 in Paris and acknowledged by the European Union, national governments and the International Maritime Organisation (IMO), require seagoing ships to significantly reduce their fuel consumption and improve their propulsion system efficiency [1,2]. At the same time, many types of ships, in particular service vessels, have to accelerate fast and accurately when performing their missions at sea [3]. For example, offshore vessels and heavy lift crane vessels require accurate dynamic positioning to perform offshore operations, ferries need to manoeuvre accurately when entering or leaving port, and naval vessels need accurate manoeuvring during combat operations.

Diesel mechanical propulsion with controllable pitch propellers can deliver both accurate manoeuvrability and high fuel efficiency during transit. Therefore, this type of propulsion is often used for the above mentioned vessels and considered in this study. A typical diesel

* Corresponding author at: Delft University of Technology, Faculty of 3ME, Building 34, Mekelweg 2, 2628CD Delft, The Netherlands.
E-mail address: r.d.geertsma@tudelft.nl (R.D. Geertsma).

http://dx.doi.org/10.1016/j.apenergy.2017.09.103
Received 3 April 2017; Received in revised form 11 September 2017; Accepted 18 September 2017
Available online 05 October 2017

Nomenclature

Greek Symbols

α	crank angle
α_Z	*Zinner* turbine area decrease factor
α_{eff}	effective angle of attack
α_i	shock free entry angle onto the leading edge of the propeller profile in deg
β	hydrodynamic pitch angle in deg
χ	the ratio between the specific heats at constant pressure and air
δ_f	fuel addition factor
ΔT	time step over which the rate is limited
η	efficiency
η_q	heat release efficiency
η_R	relative rotative efficiency of the propeller
κ	specific heat ratio
λ	air excess ratio
λ_{CR}	length ratio of the crank rod to the crank shaft radius
ω	wave radial frequency in rad/s
π	pressure ratio of turbine or compressor
Ψ_{sc}	non-dimensional scavenge flow
σ_f	stoichiometric air fuel ratio of the fuel
σ_n	cavitation number
τ_p	time constant representing pitch actuation delay in s
τ_X	fuel injection time delay in s
τ_{Pd}	time delay for filling the exhaust receiver in s
ε	parasitic heat exchanger effectiveness
ε_c	geometric compression ratio
ζ	significant wave amplitude in m

Roman symbols

$\dot{m}_t$	total mass flow at nominal conditions in kg/s
a,b,c	Seiliger parameters for isochoric, isobaric and isothermal combustion
a_η,b_η,c_η	polynomial coefficients of the turbocharger
A_{eff}	effective area of the turbine in m^2
a_{gb},b_{gb},c_{gb}	gearbox loss function parameters
c_1	Vrijdag coefficient
c_p	specific heat at constant pressure in J/kgK
C_Q,C_T	torque and thrust coefficient
c_v	specific heat at constant volume in J/kgK
D	propeller diameter in m
D_B	bore diameter in m
f_t	thrust deduction factor
f_w	wake fraction
g	standard gravity in m/s^2
h^L	lower heating value of fuel at ISO conditions in kJ/kg
i_e	number of cylinders of the engine
J	moment of inertia in kgm
k_e	number of revolutions per cycle
k_p	number of propellers
k_w	wave number in 1/m
L	length in m
L_u	unlimited lever setpoint in %
L_{set}	lever setpoint after rate limitation in %
M	torque in kNm
m	mass in cylinder in kg
m_f	fuel injected per cylinder per cycle in kg
M_i	indicated torque in kNm
	gearbox torque loss in Nm
m_{bsfc}	brake specific fuel consumption in kg/kWs
$M_{loss_{grad}}$	torque loss gradient
M_{loss}	torque loss in kNm
n	rotational speed in Hz
n_e	engine speed in Hz
n_{bld}	polytropic expansion coefficient of blowdown
n_{exp}	polytropic exponent for expansion
n_{virt}	virtual shaft speed
P	power in kW
p	pressure in Pa
p_∞	ambient water pressure at the centre-line of the propeller in Pa
P_p	propeller pitch
p_v	vapour pressure of water at ambient temperature in Pa
p_{max}	maximum cylinder pressure in Pa
P_{P0}	pitch ratio at which zero thrust is achieved
q	specific heat release in kJ/kg
Q_p	propeller torque in Nm
q_{hl}	specific heat loss in kJ/kg
R	gas constant in J/kgK
r_c	effective compression ratio
R_v	ship resistance in N
R_{CS}	crank shaft radius in m
r_{eo}	ratio of volume at Seiliger point 6 relative to 1
r_{ht}	heat transfer ratio between heating during blowdown and cooling during scavenging
R_{L+},R_{L-}	maximum, minimum increase rate of the lever setpoint
R_{P+},R_{P-}	maximum, minimum pitch increase rate
R_{Pr}	pitch reduction rate
$r_{T_{TC}}$	driving temperature ratio of the turbocharger
s_{byp}	bypass slip factor for flow around cylinder
s_{sc}	scavenge slip ratio without bypass air
s_{sl}	slip ratio of the scavenge process with bypass air
T	temperature in K
t	time in s
T_p	thrust in N
T_{bld}	*Zinner* blowdown temperature in K
T_{ev}	exhaust valve temperature in K
T_{slip}	temperature of the air slip during scavenging in K
V	cylinder volume in m^3
v_a	advance speed of water into the propeller in m/s
v_h	hydrodynamic velocity in m/s
v_s	ship speed in m/s
v_w	wakefield disturbance due to waves in m/s
w	specific work in kNm/kg
w_i	specific indicated work in Nm/kg
X	fuel pump injection in %
x_c	compression stroke effectiveness factor
X_{ct}	portion of heat released at constant temperature
X_{cv}	portion of heat released at constant volume
z	water depth in m at propeller centre

Subscripts

a	air
amb	ambient
b	after the compressor, before the intercooler
BDC	when cylinder is at bottom dead centre
c	charge air after the intercooler
com	compressor
$comb$	combustion
CR	crank rod
d	exhaust receiver
e	engine
EC	when the exhaust valve closes
EO	when the exhaust valve opens
ew	entrained water
ex	turbine exit

FAT	FAT conditions	*S*	stroke
g	exhaust gas	*s*	equilibrium
IC	when inlet valve closes	*set*	setpoint
id	assuming no heat loss	*sl*	shaftline
inl	inlet duct	*t*	total
is	assuming isentropic conditions	*TDC*	when cylinder is at top dead centre
lim	limitation	*tur*	turbine
m	mechanical	*gb*	gearbox
min	minimum	*mar*	margin
nom	nominal value	*TC*	turbocharger
p	propeller	i	state in the Seiliger cycle according to Fig. 5
ref	reference	ij	from state i to state j in the Seiliger cycle

mechanical propulsion plant consists of two turbocharged diesel engines, gearboxes, shafts and controllable pitch propellers and is illustrated in Fig. 1.

The control strategy of diesel mechanical propulsion requires a trade-off between various Measures of Effectiveness (MOEs) [4], such as fuel consumption, manoeuvrability, engine thermal loading and, in some cases, cavitation noise [5–8]. While in some circumstances, such as a transit, the objective of the control strategy will be to sail at the lowest possible fuel consumption, in other circumstances, such as manoeuvring during dynamic positioning or entering and leaving port, the objective will be to provide maximum manoeuvrability. In either case, the engine should not be thermally overloaded. Furthermore, for military vessels and ships operating in an ecologically sensitive environment, limiting radiated noise through cavitation can be an important objective. Traditional control strategies, using fixed combinator curves and engine speed control, can achieve different trade-offs by defining 2 or more different operating modes: manoeuvring mode and transit mode [9].

The assessment of the optimum trade-off for these control strategies is a complex task. The optimum trade-off could be determined during sea trails at extremely high cost. Alternatively, propulsion system models could be used to investigate the control system settings at a much lower cost [11]. However, setting up these propulsion system models requires extensive data from the equipment manufacturers and no validated models are available in literature that can be calibrated with public manufacturer data, for example information available in engine project guides [12]. Moreover, the analysis of the trade-off requires a lot of expert knowledge and the Measures of Performance (MOPs)[4] that should be considered in the control system design have not been clearly defined. This study aims to provide a propulsion system model that can be calibrated with readily available equipment data and used to compare different propulsion system architectures and their control strategies, to define MOPs to analyse propulsion and control system performance in very limited simulation time, and to analyse the improvements advanced control strategies can potentially deliver.

Diesel mechanical propulsion systems have been modelled extensively, either with very complex diesel engine models, that require an extensive analysis of parameters and exhaustive calibration [13–16], or with look-up tables that are based on extensive measurements [11,17,18]. The propulsion system model proposed in this paper is based on first principles and uses parameters obtained from publicly available manufacturers data, such as engine project guides [12] and open water propeller diagrams [19,20]. For good calibration of the engine turbocharger model, obligatory Factory Acceptance Test (FAT) data, in particular turbocharger pressures and temperatures for multiple operating points, is required. The procedure to fit parameters, described in this paper, requires FAT measurements only and do not require further heat release measurements or compressor and turbine maps, as opposed to most alternative models, which require an extensive amount of fitting parameters to achieve satisfactory performance prediction [21,22]. Because the model mimics the physical and thermodynamic behaviour, it can be used to evaluate the dynamic performance of diesel mechanical propulsion of service vessels with special interest for fuel consumption, rate of acceleration, engine thermal loading and propeller cavitation.

The contribution of this paper is threefold. First, the diesel engine model proposed in this paper is the first Mean Value First Principle (MVFP) diesel engine model that can be calibrated based on FAT measurements, without compressor and turbine maps and extensive heat release measurements as proposed in [22,23]. Moreover, it provides accurate prediction of the required MOP across the operating envelope for comparative system and control studies, as demonstrated by the presented quantitative validation with the diesel engines FAT and the ships Sea Acceptance Trials (SAT) measurements. This diesel engine model can accurately predict engine performance because the six point Seiliger cycle, an accurate turbocharger model based on *Zinner* blowdown and the *Büchi* balance, and variable turbocharger efficiency, heat release efficiency and slip ratio have been added to the model proposed in [24] to reflect the thermodynamic behaviour of modern highly turbocharged engines with *Miller* timing [25,26]. Secondly, the total ship model validation provides new insight in the influence of a control strategy on holistic performance for various MOEs. And finally, we propose benchmark manoeuvres and MOPs to quantify fuel consumption, rate of acceleration, engine thermal loading and propeller cavitation, in order to evaluate performance improvements of conventional and advanced control strategies, and compare propulsion architectures against predefined MOPs. The paper is organised as follows: We propose the propulsion system model in Section 2 and the control strategy in Section 3, to validate these models in Section 4 with FAT and SAT measurements. In Section 5, we propose benchmark MOPs and discuss the results with manoeuvring and transit mode of the proposed control strategy. Finally, we conclude and propose future work in Section 6.

2. Ship propulsion system model

The schematic representation of the diesel mechanical propulsion

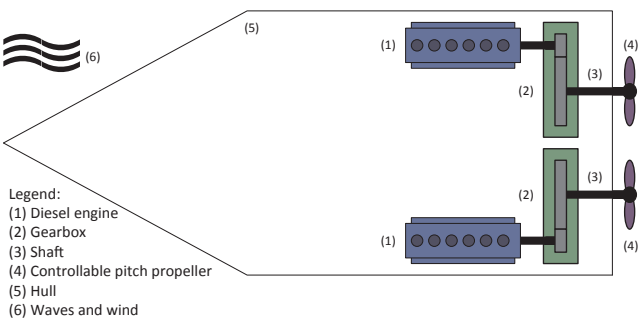

Fig. 1. Typical mechanical propulsion system layout for a naval vessel [10].

system model considered in this study is illustrated in Fig. 2. We use the modular, hierarchical and causal modelling paradigm proposed in [27], in which the direction of the arrows illustrate the causality of the coupled effort and flow variables, for example engine torque M_e with engine speed n_e, propeller torque M_p with shaft speed n_p and propeller thrust T_p with ship speed v_s. Moreover, fuel injection setpoint X_{set} and pitch ratio P_p represent control variables and wave orbital speed v_w and ship resistance function $R_v(v_s)$ represents the disturbance due to waves. Finally, the operator can control ship speed by setting control input virtual shaft speed N_{virt} in rpm. The details of the sub-models are given below.

2.1. Diesel engine model

Diesel engine models can be categorised by the level of dynamics that are considered and by the underlying physical detail, considering that the equation of motion and the associated state *engine speed* n_e are represented in the gearbox and shaftline model, as follows:

- Zero order models represent the engines torque and fuel consumption with a purely mathematical equation derived from a number of measurement points [28] or from a look-up table. Either way, the dynamics of the turbocharger are not included. Because the thermal loading of the engine mainly depends on the charge pressure, these models are not suitable to predict the thermal loading of the engine.
- First order models contain a state variable representing either the turbocharger pressure or the turbocharger speed. These models can be based on complex underlying physical models [24], on mathematical equations derived from a number of measurement points, or on look-up tables, which require even more measurement points and therefore require extensive experimental data [17, Ch. 2, pp. 16–19].
- High order Mean Value First Principle (MVFP) models include air and exhaust gas flow dynamics [13,29,22,30,31] and require an extensive set of parameters and exhaustive calibration as shown in [32]. These models mostly use the filling and emptying approach for the inlet and exhaust receiver control volumes in combination with compressor and turbine maps and require extensive calibration parameters [13,33]. Schulten and Stapersma [29] use a gas exchange model and the six point Seiliger cycle to determine the exhaust gas conditions, while [13,33] use a mathematical representation of the indicated efficiency and friction losses based on manufacturer data. When compressor and turbine maps are available, the novel approach presented in [13] can extend these maps to the low speed region, thus predicting engine behaviour at low load, for example during slow steaming.
- Zero-dimensional crank angle models determine the thermodynamic state of the air and combustion gas in the cylinder during crank angle rotation for the closed cylinder process, assuming a single homogenous ideal gas in the cylinder [14], which can be combined with a heat release model using Wiebe functions [34] as proposed in [35], with a two-zone combustion model as proposed in [36,37] or with a multi-zone combustion model as proposed in [38]. The approaches proposed in [37,38] can also predict NO_x formation using the extended Zeldovich mechanism [39] as they model the combustion process in sufficient detail.
- One-dimensional fluid dynamic models are used to predict the air flow, pressure and temperature along the flow path of the air, in the compressor, intercooler, inlet receiver, cylinder and exhaust system, including the turbine. Commercial software packages, such as GT-power and AVL Boost, estimate fluid properties along the flow, discretising the flow path, and can also address pressure waves. However, these packages require too much computational time to calculate the performance of an engine during a typical operational profile or ship manoeuvres [40,41].
- Multi-zone combustion models [38] and CFD combustion models [42] model the combustion process and the gas flow in the various engine components in three dimensions. While Raptosasios et al. [38] demonstrate multi-zone combustion models in combination with a zero-dimensional crank angle model can be used to predict NO_x production, CFD combustion models can be used to gain detailed insight into the processes of soot formation, NO_x formation, heat radiation and convective heat transfer in the cylinder during the combustion process [42]. Nevertheless, the high computational burden of these models restricts their use for extensive propulsion system analysis for multiple MOEs that occur in different timescales.

This research focusses on the dynamic performance of the diesel engine, including the thermal loading of the engine, which can be represented by the air excess ratio, turbocharger entry temperature and exhaust valve temperature [6,43]. Therefore, a MVFP has been chosen to model the diesel engine, based on the models used in [24]. In order to improve the accuracy of the prediction of the engine parameters of interest, five significant improvements are included in the model.

First, an extensive measurement campaign performed in [44] demonstrated the turbocharger pressure was overestimated in the model of [24]. Hence, we added a more accurate turbocharger model based on *Zinner* blowdown and the *Büchi* flow and power balance with a variable turbocharger efficiency, as proposed previously for a dual fuel engine in [45], a heat loss model for the turbocharger, and a third differential equation to reflect the delay in exhaust receiver pressure build-up due to receiver volume filling. Second, a fourth differential equation has been added to the model, representing the inertia of the fuel injection system and the ignition delay as proposed in [10]. Third, the six point Seiliger process has replaced the five point Seiliger process in order to more accurately predict the exhaust temperature and indicated efficiency, as proposed in [46]. Fourth, the heat release efficiency has been defined as a function of speed, to account for the longer exposure time of hot gas at lower engine speed. Finally, a variable slip ratio due to scavenging has been added, to accurately reflect the impact of *Miller* timing.

The resulting diesel engine model consists of the following sub-models: fuel pump, air swallow, heat release, Seiliger cycle, exhaust receiver and turbocharger, and mechanical conversion. In particular, the exhaust receiver and turbocharger model proposes a new modelling strategy based on *Zinner* blowdown, *Büchi* flow and power balance, the elliptic law [47,48] and a variable slip ratio assuming isentropic flow through a nozzle. The interaction of these sub-models and the equations representing their behaviour are shown in Fig. 3.

2.1.1. Fuel pump

The fuel pump model represents the time delay caused by the inertia of the fuel pump actuator and the ignition delay, as proposed in [10], as follows:

$$\frac{dm_f(t)}{dt} = \frac{m_{f_{nom}} X_{set}(t) - m_f(t)}{\tau_X}, \tag{1}$$

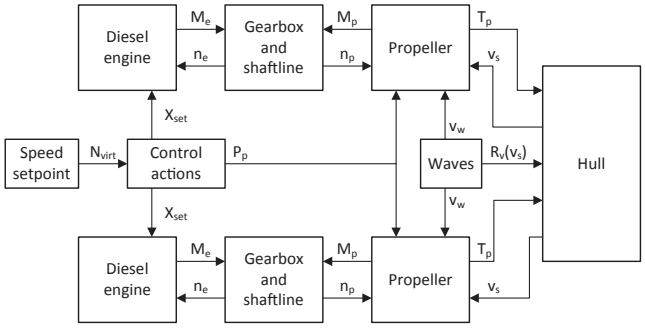

Fig. 2. Schematic presentation of direct drive propulsion system for naval vessel showing causal coupling between models.

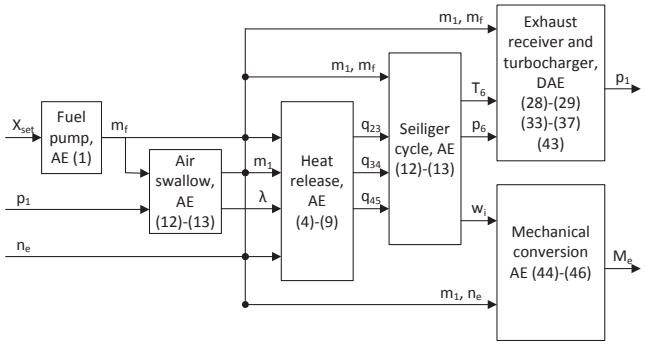

Fig. 3. Schematic presentation of the diesel engine model and the interaction between its subsystems, consisting of Algebraic Equations (AE) or Differential and Algebraic Equations (DAE).

where $m_f(t)$ is the amount of fuel injected per cylinder per engine cycle in kg, t is time in s, $m_{f_{nom}}$ is the nominal amount of fuel injected per cylinder per engine cycle in kg, X_{set} is the fuel pump injection setpoint in % of nominal fuel injection and τ_X is the fuel injection time delay in s, which can be estimated with the time required for half a stroke, which is the maximum duration of combustion, as follows:

$$\tau_X = \frac{1}{4n_{e_{nom}}}, \tag{2}$$

where $n_{e_{nom}}$ is the nominal engine speed in Hz. Fuel injection time delay in this model is assumed constant due to its small value, while a more accurate estimate could be achieved by using the actual engine speed. Furthermore, the nominal fuel injection $m_{f_{nom}}$ can be determined as follows:

$$m_{f_{nom}} = \frac{m_{bsfc_{nom}} P_{e_{nom}} k_e}{i_e n_{e_{nom}}}, \tag{3}$$

where $m_{bsfc_{nom}}$ is the nominal brake specific fuel consumption in kg/kWs, $P_{e_{nom}}$ is the nominal engine power in kW, k_e is the number of revolutions per cycle, which is 2 for a 4-stroke engine, and i_e is the number of cylinders of the engine.

2.1.2. Air swallow

The air swallow characteristics of the engine determine the air excess ratio λ, which represents the amount of air that is left after all fuel is combusted. This ratio is an important indicator for the thermal loading of the engine as discussed in [43] and can also be used to measure the effectiveness of Exhaust Gas Recirculation, as demonstrated in [30,49]. The scavenge efficiency of the engine can be assumed unity, because the model only considers 4-stroke engines with significant air slip [50, Ch. 2, p. 55]. Therefore, the air excess ratio matches the pseudo air excess ratio and can be defined as follows:

$$\lambda(t) = \frac{m_1(t)}{m_f(t)\sigma_f}, \tag{4}$$

where σ_f is the stoichiometric air fuel ratio of the fuel. Furthermore, the trapped mass at the start of compression in kg m_1 is determined by the charge air pressure p_1, using the ideal gas law, as follows:

$$m_1(t) = \frac{p_1(t)V_1}{R_a T_1}, \tag{5}$$

where V_1 is the cylinder volume at start of compression in m^3 and R_a is the gas constant of air in J/kgK. The volume V_1 is determined by the cylinder parameters as follows:

$$V_1 = \frac{\pi D_B^2 L_S r_c}{4(\varepsilon_c - 1)}, \tag{6}$$

where D_B is the bore diameter in m, L_S is the stroke length in m, ε_c is the geometric compression ratio, determined by the cylinder dimensions

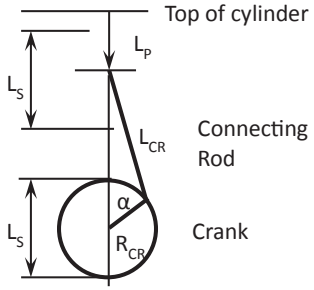

Fig. 4. Schematic view of the geometry of cylinder, crank rod and crank shaft [51 Ch. 14, p. 632].

and r_c is the effective compression ratio, which is determined by the inlet valve timing and can be calculated as follows [51, Ch. 14, pp. 632–633]:

$$r_c = (\varepsilon_c - 1)x_c + 1 \tag{7}$$

$$x_c = \frac{L_{IC}}{L_{BDC}} \tag{8}$$

$$L_{IC} = L_S\left(\frac{1}{\varepsilon_c - 1} + \frac{1}{2}\left((1 - \cos\alpha_{IC}) + \frac{1}{\lambda_{CR}}(1 - r_{tg})\right)\right) \tag{9}$$

$$r_{tg} = \sqrt{1 - \lambda_{CR}^2 \sin^2\alpha_{IC}} \tag{10}$$

$$\lambda_{CR} = \frac{L_S}{2L_{CS}} \tag{11}$$

$$L_{BDC} = \frac{\varepsilon L_S}{\varepsilon - 1}, \tag{12}$$

where x_c is the compression stroke effectiveness factor, L_{IC} is the distance between the top of the cylinder and the piston crown, *cylinder space length* L_p in Fig. 4, in m when the inlet valve closes, L_{BDC} is the cylinder space length in m when the cylinder is at bottom dead centre (BDC) position, L_{TDC} is the cylinder space length in m when the cylinder is at top dead centre (TDC) position, L_{CR} is the length of the crank rod in m, α_{IC} is the crank angle when the inlet valve closes, λ_{CR} is the length ratio of the crank rod to the crank shaft radius in m R_{CR} and r_{tg} is a trigonometric root used to split the equation.

2.1.3. Heat release

The heat release model represents the heat release during the isochoric, isobaric and isothermal combustion stages of the six point Seiliger process. The released heat is assumed to be split between a constant volume segment q_{23} in kJ/kg, a constant pressure segment q_{34} in kJ/kg, and a constant temperature segment q_{45}, according to [15], as follows:

$$q_{23}(t) = X_{cv}(t)\frac{m_f(t)\eta_q(t)\eta_{comb}h^L}{m_1(t)} \tag{13}$$

$$q_{34}(t) = (1 - X_{cv}(t) - X_{ct}(t))\frac{m_f(t)\eta_q(t)\eta_{comb}h^L}{m_1(t)} \tag{14}$$

$$q_{45}(t) = X_{ct}(t)\frac{m_f(t)\eta_q(t)\eta_{comb}h^L}{m_1(t)}, \tag{15}$$

where X_{cv} is the portion of heat released at constant volume, X_{ct} is the portion of heat released at constant temperature, η_q is the heat release efficiency, η_{comb} is the combustion efficiency and h^L is the lower heating value of fuel at ISO conditions in kJ/kg. The combustion efficiency is considered a function of air excess ratio λ, according to [52], but is unity within the engine operating limits. The nominal heat release efficiency η_q is estimated using nominal engine parameters and (5), (17)–(23) and (53)–(55). Furthermore, the percentage of heat lost is

considered inversely related to engine speed in Hz n_e, as follows:

$$\eta_q(t) = 1-(1-\eta_{q_{nom}})\frac{n_{e_{nom}}}{n_e(t)}. \tag{16}$$

The constant volume portion of combustion X_{cv} is considered to increase linearly with engine speed at a negative rate $X_{cv_{grad}}$, and the constant temperature portion of combustion X_{ct} is considered to increase proportional to fuel injection, as follows:

$$X_{cv}(t) = X_{cv_{nom}} + \frac{n_e(t)-n_{e_{nom}}}{n_{e_{nom}}}X_{cv_{grad}} \tag{17}$$

$$X_{ct}(t) = X_{ct_{nom}}\frac{m_f(t)}{m_{f_{nom}}}, \tag{18}$$

where $X_{ct_{nom}}$ is the nominal constant temperature portion, and $X_{cv_{nom}}$ is the nominal constant volume portion, which can be estimated from the maximum cylinder pressure in the nominal working point $p_{max_{nom}}$ in Pa, which often is available in engine project guides, as follows:

$$X_{cv_{nom}} = \frac{c_{v_a}T_1 r_c^{\kappa_a-1}\left(\frac{p_{max_{nom}}}{p_{1_{nom}}r_c^{\kappa_a}}-1\right)m_{1_{nom}}}{\eta_q(t)m_{f_{nom}}h^L}, \tag{19}$$

where c_{v_a} is the specific heat at constant volume of air in J/kgK, T_1 is the air temperature in the cylinder at the start of compression in K, κ_a is the specific heat ratio of air, $p_{1_{nom}}$ is the nominal charge air pressure in Pa and $m_{1_{nom}}$ is the nominal trapped mass at the start of compression in kg. Finally, the air temperature at start of compression T_1 in K is assumed constant and can be estimated according to [48, Ch. 6, p. 274], as follows:

$$T_1 = T_c + \varepsilon_{inl}(T_{inl}-T_c), \tag{20}$$

where T_c is the charge air temperature after the intercooler in K, ε_{inl} is the parasitic heat exchanger effectiveness of the heat exchange between inlet duct and the air and T_{inl} is the temperature of the inlet duct that heats the inducted air in K. Because the charge air temperature is fairly constant and the temperature is an estimate, all these temperatures are assumed constant.

2.1.4. Seiliger cycle

The six stage Seiliger process consists of polytropic compression, isochoric combustion, isobaric combustion, isothermal combustion and polytropic expansion and can be used to determine the work produced during the closed cylinder process and establish the exhaust gas properties at the end of expansion [50]. Moreover, we assume the gas is a perfect gas with a homogeneous composition. This cycle is illustrated in Fig. 5. The associated equations are summarised in Table 1 [50, Ch. 3, p. 136–137], where V_i, p_i and T_i are the volume in m^3, pressure in Pa and temperature in K at state i, w_{ij} and q_{ij} are the specific work in kNm/kg and specific heat in kJ/kg produced during the process from state i to state j, a, b and c are the Seiliger parameters as defined in [50], $c_{p,a}$ is the specific heat at constant pressure for air in J/kgK, n_{exp} is the polytropic exponent for expansion, as polytropic expansion allows for jacket water cooling, and r_{eo} is the ratio of the volume at Seiliger point 6, when the exhaust valve opens, to point 1, when the inlet valve closes, which is determined by the exhaust valve opening angle α_{EO}, using (9), as follows:

$$r_{eo} = \frac{L_{EO}}{L_{IC}} \tag{21}$$

$$L_{EO} = L_S\left(\frac{1}{\varepsilon_c-1} + \frac{1}{2}\left((1-\cos\alpha_{EO}) + \frac{1}{\lambda_{CR}}(1-r_{lg})\right)\right), \tag{22}$$

where L_{EO} is the cylinder space length when the exhaust valve opens. The total indicated work can then be determined from the work of the Seiliger stages in Table 1, as follows:

$$w_i = w_{12} + w_{34} + w_{45} + w_{56}. \tag{23}$$

2.1.5. Exhaust receiver and turbocharger

The process of blow down after the exhaust valve opens, gas expelling during the exhaust stroke, and scavenging after the inlet opens can be represented by *Zinner* blowdown, as proposed by [53] and extensively discussed in [48], as follows:

$$T_{bld}(t) = \left(\frac{1}{n_{bld}} + \frac{(n_{bld}-1)}{n_{bld}}\frac{p_{d,s}(t)}{p_6(t)}\right)T_6(t), \tag{24}$$

where T_{bld} is the *Zinner* blowdown temperature in K, n_{bld} is the polytropic expansion coefficient of the blowdown process, allowing for heat loss to the cylinder, exhaust valve and duct, and $p_{d,s}$ is the equilibrium pressure in the exhaust receiver in Pa.

The resulting exhaust receiver temperature T_d in K after mixing of the air fuel mixture expelled from the cylinder and the scavenge air that slips through the cylinder, can be defined as follows [48]:

$$T_d(t) = \frac{c_{p_g}T_{bld}(t)(m_1(t)+m_f(t)) + c_{p_a}T_{slip}s_{sl}(t)m_1(t)}{c_{p_g}(m_1(t)+m_f(t)) + c_{p_a}s_{sl}(t)m_1(t)}, \tag{25}$$

where c_{p_g} is the specific heat at constant pressure for the exhaust gas in J/kgK, s_{sl} is the slip ratio of the scavenge process as defined in [48, Ch. 2] and T_{slip} is the temperature of the air slip during scavenging in K, which can be estimated using (20). The nominal slip ratio of the scavenge process $s_{sl_{nom}}$ can be estimated from the total mass flow at nominal conditions $\dot{m}_{t_{nom}}$ in kg/s, as follows:

$$s_{sl_{nom}} = \frac{\dot{m}_{t_{nom}}-(\dot{m}_{1_{nom}}-\dot{m}_{f_{nom}})}{\dot{m}_{1_{nom}}} \tag{26}$$

$$\dot{m}_{1_{nom}} = \frac{p_{1_{nom}}V_1 i_e n_e}{R_a T_1 k_e} \tag{27}$$

$$\dot{m}_{f_{nom}} = m_{bsfc_{nom}}P_{nom}, \tag{28}$$

where $\dot{m}_{1_{nom}}$ is the trapped mass flow of all cylinders at nominal conditions in kg/s and $\dot{m}_{f_{nom}}$ is the nominal fuel mass flow in kg/s. Subsequently, the slip ratio can be represented as follows, as proposed in [48, Ch. 6]:

$$s_{sl}(t) = s_{sl_{nom}}\frac{n_{e_{nom}}}{n_e(t)}\frac{m_{1_{nom}}}{m_1(t)}\frac{p_1(t)}{p_{1_{nom}}}\frac{\Psi_{sc}(t)}{\Psi_{sc_{nom}}} \tag{29}$$

$$\Psi_{sc}(t) = \sqrt{\frac{2\kappa_g}{\kappa_g-1}}\sqrt{\left(\frac{p_d(t)}{p_1(t)}\right)^{\frac{2}{\kappa_g}} - \left(\frac{p_d(t)}{p_1(t)}\right)^{\frac{\kappa_g+1}{\kappa_g}}}, \tag{30}$$

where κ_g is the specific heat ratio of the exhaust gas, $m_{1_{nom}}$ is the trapped mass at nominal conditions in kg, which can be determined with (5), and Ψ_{sc} is the non-dimensional scavenge flow, assuming isentropic flow through a nozzle and choking above the critical

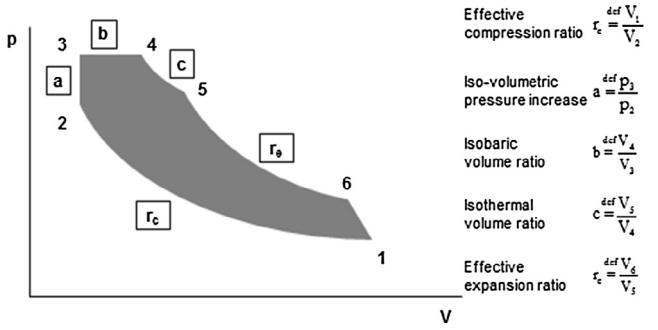

Fig. 5. Typical six point Seiliger or dual cycle in pressure (p) – volume (V) plot, consisting of compression (1–2), isochoric combustion (2–3), isobaric combustion (3–4), isothermal combustion (4–5) and expansion (5–6), from [50].

Table 1
Seiliger cycle equations [50, Ch. 3 pp.136-137].

Seiliger stage	Volume V	Pressure p	Temperature T	Specific work w	Heat q
Compression 1–2	$\frac{V_1}{V_2} = r_c$	$\frac{p_2}{p_1} = r_c^{\kappa a}$	$\frac{T_2}{T_1} = r_c^{(\kappa a-1)}$	$w_{12} = \frac{R_a(T_2-T_1)}{\kappa a-1}$	–
Isochoric combustion 2–3	$\frac{V_3}{V_2} = 1$	$\frac{p_3}{p_2} = a$	$\frac{T_3}{T_2} = a$	–	$q_{23} = c_{v,a}(T_3-T_2)$
Isobaric combustion 3–4	$\frac{V_4}{V_3} = b$	$\frac{p_4}{p_3} = 1$	$\frac{T_4}{T_3} = b$	$w_{34} = R_a(T_4-T_3)$	$q_{34} = c_{p,a}(T_4-T_3)$
Isothermal combustion 4–5	$\frac{V_5}{V_4} = c$	$\frac{p_4}{p_5} = c$	$\frac{T_5}{T_4} = 1$	$w_{45} = R_a T_4 \ln c$	$q_{45} = R_a T_4 \ln c$
Expansion 5–6	$\frac{V_6}{V_5} = \frac{r_{eo} r_c}{bc}$	$\frac{p_5}{p_6} = \left(\frac{r_{eo} r_c}{bc}\right)^{nexp}$	$\frac{T_5}{T_6} = \left(\frac{r_{eo} r_c}{bc}\right)^{nexp-1}$	$w_{45} = \frac{R_a(T_6-T_5)}{(nexp-1)}$	–

pressure, as discussed extensively in [48]. Moreover, the case study engine has a bypass valve to create additional flow around the cylinder to increase air flow in the turbocharger at low engine speed. This is represented by a bypass slip factor s_{byp} that is multiplied with the scavenge slip ratio s_{sc} to obtain the total slip ratio s_{sl}.

The pressure before the turbine is determined by the air swallow characteristics of the turbine. This model uses the elliptic law as derived in [47, Ch. 4, p. 122–124] and discussed in [48, Ch. 8, p. 363–410] to estimate the equilibrium pressure in the exhaust receiver $p_{d,s}$ in Pa, as follows:

$$p_{d,s}(t) = \sqrt{\frac{(s_{sl}(t)\dot{m}_1(t) + \dot{m}_f(t))^2 R_g T_d(t)}{\alpha_Z^2 A_{eff}^2} + p_{ex}^2} \tag{31}$$

$$\dot{m}_1(t) = m_1(t) i_e \frac{n_e(t)}{k_e} \tag{32}$$

$$\dot{m}_f(t) = m_f(t) i_e \frac{n_e(t)}{k_e}, \tag{33}$$

where $\dot{m}_1$ is the trapped mass flow in kg/s, $\dot{m}_f$ is the fuel mass flow in kg/s, R_g is the gas constant of the exhaust gas in J/kgK, α_Z is the *Zinner* turbine area decrease factor, which is assumed one for a constant pressure turbocharger, A_{eff} is the effective area of the turbine in m^2 and p_{ex} is the pressure after the turbocharger in Pa, which is assumed to be atmospheric pressure, neglecting exhaust pressure losses. The effective turbocharger area is estimated with (31) for nominal conditions. Substituting (24) in (25), (30) in (29), and (29) in (25) and (31), the quadratic system of Eqs. (25) and (31) can be solved explicitly.

We assume a time delay τ_{Pd} for filling the exhaust receiver, because it measures a considerable volume. Thus, the pressure in the exhaust receiver p_d in Pa can be expressed as follows:

$$\frac{dp_d(t)}{dt} = \frac{p_{d,s}(t) - p_d(t)}{\tau_{Pd}}. \tag{34}$$

The equilibrium turbocharger pressure ratio π_{com_s}, can be estimated from the pressure and temperature in the exhaust receiver from the *Büchi* power and flow balance, Eq. (35), as discussed in [48, Ch. 8]. The losses in the inlet duct, filter and air cooler are neglected. This leads to the following set of equations:

$$\pi_{com_s}(t) = \left(1 + \delta_f(t)\chi_g \eta_{TC}(t) r_{T_C}(t)\left(1 - \frac{1}{\pi_{tur}(t)^{\left(\frac{\kappa g-1}{\kappa g}\right)}}\right)\right)^{\left(\frac{\kappa a-1}{\kappa a}\right)} \tag{35}$$

$$\pi_{com_s}(t) = \frac{p_{1,s}(t)}{p_{amb}} \tag{36}$$

$$\delta_f(t) = 1 + \frac{m_f(t)}{(1+s_{sl})m_1(t)} \tag{37}$$

$$r_{T_C}(t) = \frac{T_d(t)}{T_{amb}} \tag{38}$$

$$\pi_{tur}(t) = \frac{p_d(t)}{p_{ex}}, \tag{39}$$

where δ_f is the fuel addition factor, χ_g is the ratio between the specific heats at constant pressure of the exhaust gas c_{p_g} and of air c_{p_a}, η_{TC} is the turbocharger efficiency, r_{T_C} is the driving temperature ratio of the turbocharger, $p_{1,s}$ is the equilibrium turbocharger pressure at a static working point in Pa, p_{amb} and T_{amb} are the ambient pressure in Pa and temperature in K, because the inlet duct, filter and air cooler pressure losses are neglected and π_{tur} is the turbine pressure ratio. The variable turbocharger efficiency is represented with a quadratic function of charge pressure, as follows [45]:

$$\eta_{TC}(t) = a_\eta + b_\eta p_1(t) + c_\eta p_1^2(t), \tag{40}$$

where a_η, b_η and c_η are the polynomial coefficients of the turbocharger for estimating the turbocharger efficiency η_{TC}. The coefficients are estimated from the FAT load P_{FAT} in kW, speed n_e in rev/s, charge pressure p_1 in Pa and fuel consumption m_{bsfc} in g/kWh, Table 1, and (3), (25), (31) and (35). The first order time delay of the turbocharger reaching equilibrium speed and pressure p_1 in Pa, due to it's inertia, is represented by a time delay τ_{TC}, as follows:

$$\frac{dp_1(t)}{dt} = \frac{p_{1,s}(t) - p_1(t)}{\tau_{TC}}. \tag{41}$$

The turbine exit temperature T_{ex} is determined from the exhaust receiver temperature T_d, using the isentropic turbine efficiency $\eta_{tur_{is}}$ and specific heat loss q_{hl} in kJ/kg, as follows:

$$T_{ex_{is}}(t) = T_d(t)\left(\frac{p_{ex}(t)}{p_d(t)}\right)^{\left(\frac{\kappa g-1}{\kappa g}\right)} \tag{42}$$

$$T_{ex_{id}}(t) = T_d(t) + \eta_{tur_{is}}(t)(T_{ex_{is}}(t) - T_d(t)) \tag{43}$$

$$T_{ex}(t) = T_{ex_{id}}(t) - \frac{q_{hl}(t)}{c_{p_g}}, \tag{44}$$

where $T_{ex_{is}}$ is the isentropic turbine exhaust temperature, and $T_{ex_{id}}$ is the

ideal turbine exhaust temperature, including turbine losses without heat loss. The specific heat loss q_{hl} is considered to be linearly dependant on the temperature difference between the turbine entry temperature T_d and ambient temperature T_{amb} and linearly dependant on the reciproke of the mas flow $\dot{m}_t$, as Fourier's law dictates that heat loss depends on temperature flux and residence time, as follows:

$$q_{hl}(t) = q_{hl_{nom}} \frac{(T_d(t) - T_{amb})}{(T_{d_{nom}} - T_{amb})} \frac{\dot{m}_{t_{nom}}}{\dot{m}_t(t)}, \tag{45}$$

where $q_{hl_{nom}}$ is the nominal specific heat loss determined from FAT measurements using (42)–(44) and the following equations for specific compressor and turbine work w_{com} and w_{tur}:

$$w_{com}(t) = c_{p_a}(T_b(t) - T_{amb}) \tag{46}$$

$$w_{tur}(t) = \frac{w_{com}(t)}{\delta_f(t)\eta_{com_m}} \tag{47}$$

$$w_{tur}(t) = c_{p_g}(T_{ex_{id}}(t) - T_d(t)), \tag{48}$$

where T_b is the temperature after the compressor in K and η_{com_m} is the mechanical turbocharger efficiency which is considered constant. The isentropic turbine efficiency $\eta_{tur_{is}}$ is determined using a quadratic fit from FAT measurements as in (40) based on the following equations:

$$\eta_{tur_{is}}(t) = \frac{T_{ex_{id}}(t) - T_d(t)}{T_{ex_{is}}(t) - T_d(t)} \tag{49}$$

$$\eta_{tur_{is}}(t) = a_{\eta_t} + b_{\eta_t} p_1(t) + c_{\eta_t} p_1^2(t), \tag{50}$$

where a_{η_t},b_{η_t} and c_{η_t} are the polynomial coefficients of the isentropic turbine efficiency. Finally, the exhaust valve temperature T_{ev} can be estimated using the heat transfer mechanism between the exhaust gasses and exhaust valve during blowdown and scavenging as proposed in [5], as follows:

$$T_{ev}(t) = \frac{T_6(t) + r_{ht}(t)T_1}{1 + r_{ht}(t)} \tag{51}$$

$$r_{ht}(t) = s_{sc}(t)^{0.8}\left(\frac{T_1}{T_6(t)}\right)^{0.25}\left(\frac{\alpha_{EC} - \alpha_{IO}}{\alpha_{IO} - \alpha_{EC}}\right)^{0.2}, \tag{52}$$

where r_{ht} is the heat transfer ratio between heating during blowdown and cooling during scavenging, α_{IO} is the inlet valve opening angle, α_{EC} is the exhaust valve closing angle, and s_{sc} is the scavenge slip ratio without multiplication of bypass slip factor s_{byp} as the bypass flow does not cool the exhaust valve.

2.1.6. Mechanical conversion

The conversion from indicated work in the cylinder to mechanical torque on the output shaft of the diesel engine leads to a torque loss M_{loss} in kNm that is represented with a linear loss model, as follows:

$$M_e(t) = M_i(t) - M_{loss}(t) \tag{53}$$

$$M_i(t) = \frac{w_i(t)m_1(t)i_e}{k_e 2\pi} \tag{54}$$

$$M_{loss}(t) = M_{loss_{nom}}\left(1 + M_{loss_{grad}}\frac{n_{e_{nom}} - n_e(t)}{n_{e_{nom}}}\right), \tag{55}$$

where M_e is engine torque in kNm, M_i is the indicated torque in kNm, $M_{loss_{nom}}$ is the nominal torque loss in kNm and $M_{loss_{grad}}$ is the torque loss gradient. This approach assumes mechanical losses are independent of engine load, which is limitedly accurate. Alternatively, [54] demonstrated that friction can be accurately modelled as a function of mean piston speed and mean effective pressure, which is directly related to the load. However, for this approach sufficient empirical data is required, which is not available for the case study. Future improvement of the proposed diesel engine model could focus on implementing [54].

Finally, the first order equation of motion for engine rotation determines the engine speed, as mentioned at the start of this section. Because we consider the engine, gearbox, shaft-line and propeller to be rigidly coupled, the equation of motion for the rotation of this complete assembly is included in the gearbox and shaft-line model, as illustrated in Fig. 2.

2.2. Gearbox and shaft-line model

Literature on modelling of maritime gearbox losses is very limited, even though gearbox losses as a general subject has received renewed interest due to numerical modelling techniques [55]. Models on maritime gearbox losses consist of either a complex thermal network model [56] or a simple gearbox loss function such as the ones in [10,56,57]. While the thermal network model is based on non-dimensional heuristic estimation models for the various loss sources in the gearbox, it requires very detailed design information of the gearbox, which often is only available for the gearbox designer.

[56] has shown that the linear torque loss model proposed in his work can accurately predict gearbox losses calculated with a thermal network model if calibrated correctly. However, [56] proposes to use alternative parameters to predict the efficiency on the propeller curve and the generator (constant speed) line. Alternatively, we use values at both the propeller curve and the generator line to predict the gearbox torque losses across the full gearbox operating envelope. As a result, the gearbox torque loss in Nm and the resulting gearbox output torque M_{gb} in Nm can be represented as follows:

$$M_l(t) = M_{l_{nom}}\left(a_{gb} + b_{gb}\frac{n_e(t)}{n_{e_{nom}}} + c_{gb}\frac{M_e(t)}{M_{e_{nom}}}\right) \tag{56}$$

$$M_{l_{nom}} = \frac{P_{l_{nom}}}{n_{p_{nom}}} \tag{57}$$

$$M_{gb}(t) = M_e(t)i_{gb} - M_l(t), \tag{58}$$

where $M_{l_{nom}}$ is the nominal gearbox torque loss in Nm, a_{gb},b_{gb} en c_{gb} are the gearbox loss function parameters, $P_{l_{nom}}$ is the nominal gearbox loss power in W and $n_{p_{nom}}$ is the nominal gearbox output shaft speed and thus the nominal propeller speed in rev/s. All these parameters can be determined from manufacturer data or from a thermal network model as proposed in [56].

Apart from the gearbox losses, the shaft bearings cause additional losses. We assume these shaft-line losses M_{sl} in Nm to depend solely on the gearbox torque M_{gb} in Nm, as follows:

$$M_{sl}(t) = \eta_{sl}M_{gb}(t), \tag{59}$$

where η_{sl} is the shaft line efficiency.

Finally, we represent the equation of motion for the engine, gearbox, shaft-line and propeller, which are assumed to be rigidly coupled, as follows:

$$\frac{dn_p(t)}{dt} = \frac{M_{gb(t)} - M_{sl(t)} - M_p(t)}{2\pi J_t} \tag{60}$$

$$J_t = J_e i_{gb}^2 + J_{gb} + J_{sl} + J_p + J_{ew}, \tag{61}$$

where n_p is the propeller and shaft-line speed in rev/s, J_t is the total moment of inertia of the shaft and all connected rotating equipment reflected to propeller speed in kgm^2, J_e is the moment of inertia of the diesel engine in kgm^2, J_{gb} is the moment of inertia of the gearbox in kgm^2, J_{sl} is the moment of inertia of the shaft-line in kgm^2, J_p is the moment of inertia of the propeller in kgm^2 and J_{ew} is the moment of inertia of the entrained water in kgm^2.

2.3. Propeller model

The first goal of the propeller model is to predict the thrust, torque and efficiency characteristics as a function of propeller pitch, and

propeller and ship speed. We use the well established open water test results. In order to allow for reverse thrust, we use the four quadrant open water diagrams, which are widely available for typical propellers, for example in the Taylor and Gawn Series [58,59], the most widely used Wageningen B and Ka-series [20] and the recently developed Wageningen C- and D-series for Controllable Pitch Propellers (CPPs) [60,19].

In order to use the four quadrant open water diagrams, we first have to express the hydrodynamic pitch angle β in deg as a function of shaft speed n_p in rev/s, ship speed v_s in m/s and wakefield disturbance due to waves v_w in m/s, as follows:

$$v_a(t) = v_s(t)(1-f_w) + v_w(t) \tag{62}$$

$$\beta(t) = arctan\left(\frac{v_a(t)}{0.7\pi n_p(t)D}\right), \tag{63}$$

where v_a is the advance speed of the water relative to the propeller in m/s, f_w is the wake fraction, which is considered constant and D is the propeller diameter in m.

The open water diagrams, which in the Wageningen C and D series have been made available in 40th order Fourier series, linearly truncated from the 31st harmonic to the 40th harmonic, provide the associated torque and trust coefficients C_Q and C_T as a function of propeller pitch to diameter ratio P_p at 70% of the radius in m and the hydrodynamic pitch angle β in deg [19]. The torque Q_p in Nm and thrust T_p in N are represented by the torque and thrust coefficients C_Q and C_T, as follows:

$$v_h(t) = \sqrt{v_a(t)^2 + (0.7\pi n_p(t)D)^2} \tag{64}$$

$$T_p(t) = C_T(t)\frac{1}{2}\rho v_h(t)^2\frac{\pi}{4}D^2 \tag{65}$$

$$Q_p(t) = C_Q(t)\frac{1}{2}\rho v_h(t)^2\frac{\pi}{4}D^3, \tag{66}$$

where v_h is the hydrodynamic velocity in m/s. In order to obtain the actual propeller torque M_p in Nm, the relative rotative efficiency of the propeller η_R, which is assumed constant, needs to be accounted for [61]:

$$M_p(t) = \frac{Q_p(t)}{\eta_R}. \tag{67}$$

Because we consider a CPP, the time delay between changing the pitch setpoint and the actual movement of the pitch needs to be accounted for Grimmelius and Wesselink [62–64] performed an extensive analysis on the non-linear behaviour of the forces in a CPP and in the CPP actuating mechanism and [65,16,66] have derived a detailed non-linear model for the pitch actuation mechanism of a CPP and included this in a propulsion simulation model. However, in this study, we assume a first order system with time constant τ_P to represent the actuation delay due to friction, oil leakage, pressurising and inertia in the pitch actuation system, because [62] has shown a first order linear system can provide insight in the overall system behaviour as opposed to the behaviour of the CPP actuation mechanism and the associated wear. This leads to the following model equations:

$$\frac{dP_p(t)}{dt} = \frac{P_{p_{set}}(t)-P_p(t)}{\tau_P}, \tag{68}$$

where $P_{p_{set}}$ is the pitch ratio setpoint from the controller.

The second goal of the propeller model is to assess the influence of the control system strategy on the cavitation behaviour of the propeller. A wealth of research is available on the design of propellers and the use of cavitation tunnels and full scale measurements to determine the propeller cavitation behaviour and optimise its design. An extensive review on cavitation research is reported in [67]. More recently, application of Computational Fluid Dynamics (CFD) has allowed to optimise propeller design based on numerical analysis [68]. However, for the purpose of dynamic simulation models, CFD is too detailed and computationally expensive.

Alternatively, Vrijdag [7,17] proposes to use the effective angle of attack α_{eff} in combination with an experimentally determined cavitation bucket of a propeller as a measure of the likelihood of cavitation occurring. The definition of the effective angle of attack α_{eff} and the reasoning behind this definition is extensively described in [7,17] and is as follows:

$$\alpha_{eff}(t) = \arctan\left(\frac{P_p}{0.7\pi D}\right) - \arctan\left(\frac{c_1 v_a}{0.7\pi n_p D}\right) - \alpha_i, \tag{69}$$

where α_i is the shock free entry angle onto the leading edge of the propeller profile in deg, and c_1 is the *Vrijdag* coefficient to calibrate the effective angle of attack with the centre point of the cavitation bucket such that the cavitation bucket can be represented as two lines in the $\alpha_{eff}-\sigma_n$ phase plane. [17, Ch. 7, pp. 115–120] describes the procedure to determine c_1 and [17, Ch. 7, pp. 147–159] describes the schematic cavitation bucket in the $\alpha_{eff}-\sigma_n$ phase plane, with the cavitation number σ_n defined as follows:

$$\sigma_n = \frac{p_\infty - p_v}{1/2\rho n_p^2 D^2}, \tag{70}$$

where p_∞ is the ambient water pressure at the centre-line of the propeller in Pa and p_v is the vapour pressure of water at the ambient temperature in Pa. After experimentally determining the cavitation bucket, Vrijdag [17] has developed a control strategy that is aimed at maintaining the angle of attack near its optimum value and demonstrates its effectiveness in the $\alpha_{eff}-\sigma_n$ phase plane. This type of plot will be referred to as a *cavitation plot* in the remainder of this paper.

2.4. Hull model

The proposed model analyses ship motion only in surge direction, as opposed to more complex 6 degree of freedom models proposed in [15,69]. Therefore, the hull model needs to provide an estimate of the ships resistance R_v in N as a function of speed v_s in kts. The two most used methods to determine the ship resistance are the estimation of the ship resistance with semi-empirical methods such as [70] and the measurement of the ship resistance in a towing tank test. For this study, tow test measurement were used that were corrected for environmental conditions and fouling [71].

Subsequently, the equation of motion represents the ship manoeuvring dynamics in one degree of freedom, as follows:

$$\frac{dv_s(t)}{dt} = \frac{\left(k_p T_p(t) - \frac{R_v(v_s(t))}{1-f_t}\right)}{m}, \tag{71}$$

where k_p is the number of propellers, f_t is the thrust deduction factor, which is assumed constant and m is the ships mass in kg, neglecting the added mass due to the boundary layer.

2.5. Wave model

Waves can cause serious disturbances on the loading of diesel engines when a ship sails in high sea states, particularly when the engine runs in speed control. [8] has documented measurements on a *Karel Doorman* class frigate sailing in head waves in Sea State 6, which is the worst case scenario within normal operations according to typical design specifications. These measurements, shown in Fig. 6, clearly illustrate how the disturbance of waves can cause engine overloading.

The main cause of the disturbance on engine loading is the fluctuating wake speed of the water flowing into the propeller, as previously discussed in [10]. The orbital movement of water causes a disturbance on the average speed of the water entering the propeller, an exponential distribution of water speed along the depth of the propeller and an

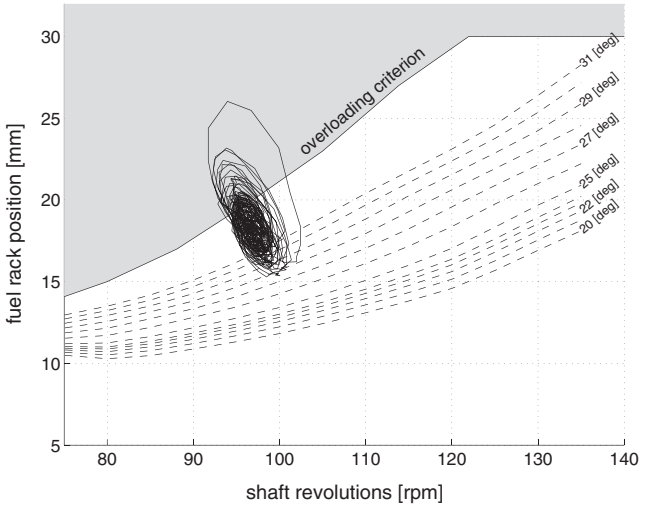

Fig. 6. Engine speed and fuel rack measurements of diesel direct propulsion in Sea State 6 head waves, plotted in the phase plane, with constant pitch lines in degrees (deg), violating the engine overloading criterion ©IFAC 2001 [8].

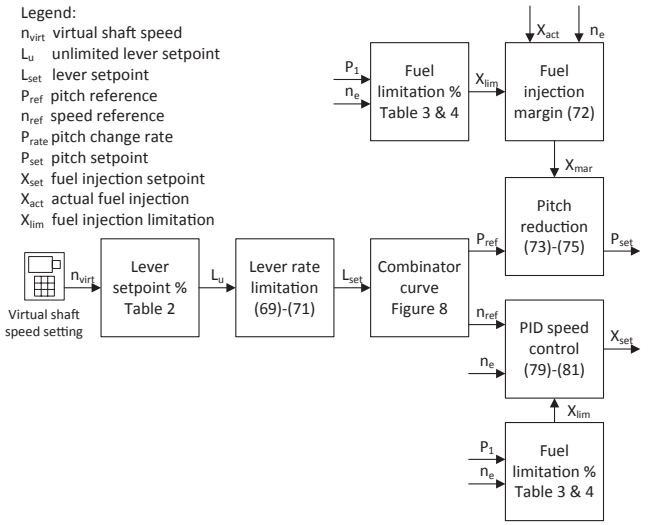

Fig. 7. Schematic representation of baseline control strategy for diesel mechanical propulsion with CPP.

oblique inflow. In this study, we are interested in the significant disturbance of the wave orbital movement on the propeller loading, due to the significant wave height [72,73]. We therefore consider the wave speed at the propeller centre, as follows:

$$v_w(t) = \zeta\omega e^{k_w z} sin((-kv_s-\omega)t) \tag{72}$$

$$k_w = \frac{\omega^2}{g}, \tag{73}$$

where ζ is the significant wave amplitude in m, ω is the wave radial frequency in rad/s, k_w is the wave number in 1/m, z is the water depth in m at the propeller centre and g is the standard gravity in m/s^2.

In summary, the ship propulsion system model consists of 4 sub-models with a system of Differential and Algebraic Equations (DAEs) and the wave sub-model with an Algebraic Equation (AE), with the relations shown in Fig. 2. The model consists of 6 state variables: fuel injection per cylinder per cycle m_f, charge pressure p_1, exhaust receiver pressure p_d, propeller speed n_p, propeller pitch P_p and ship speed v_s. The overall system is thus composed of the diesel engine DAEs (1), (4), (5), (13)–(18), Table 1, (21)–(25) and (29)–(55), the gearbox DAEs (56) and (58)–(60), the propeller DAEs (62)–(68), the hull DAE (71) and the wave AE (72).

3. Conventional control

3.1. Control objectives

The objective for the conventional control strategy is to represent the control system implemented on the case study, the *Holland* class patrol vessel. The control objectives for this baseline control strategy, used to validate the propulsion system model, are:

- Provide requested virtual shaft speed n_{virt} as defined in [7]:

$$n_{virt}(t) = \frac{P_p(t)-P_{p_0}}{P_{p_{nom}}-P_{p_0}} n_p, \tag{74}$$

  where P_{p_0} is the pitch ratio at which zero thrust is achieved and $P_{p_{nom}}$ is the nominal pitch ratio.
- Prevent engine overloading in design conditions by limiting the telegraph position acceleration rate, limiting the pitch increase rate as a function of virtual shaft speed and reducing pitch when the engine margin is too small.
- Provide high manoeuvrability within engine overloading limitations in manoeuvring mode for design conditions.
- Provide high propulsion efficiency within engine overloading limitations in transit mode for design conditions.

3.2. Control system design

An extensive review on the control strategies used for mechanical propulsion is available in [9]. While some alternative strategies have been proposed, the basic principle for control of mechanical propulsion with CPPs remains speed control of the engine in combination with one or two fixed combinator curves [74,8,75]. The schematic representation of the baseline control strategy used for validation is given in Fig. 7.

The virtual shaft speed setpoint $n_{virt_{set}}$ in rpm is converted in an unlimited lever setpoint L_u in % with linear interpolation, according to Table 2. Subsequently, the increase rate of the lever setpoint is limited to limit engine thermal loading, as follows:where L_{set} is the setpoint

$$\begin{aligned} &L_u(t)-L_{set}(t-\Delta T) > R_{L+}\Delta T: \\ &L_{set}(t) = L_{set}(t-\Delta T) + R_{L+}\Delta T \end{aligned} \tag{75}$$

$$\begin{aligned} &R_{L-} \leqslant L_u(t)-L_{set}(t-\Delta T) \leqslant R_{L+}: \\ &L_{set}(t) = L_u(t) \end{aligned} \tag{76}$$

$$\begin{aligned} &L_u(t)-L_{set}(t-\Delta T) < R_{L-}\Delta T: \\ &L_{set}(t) = L_{set}(t-\Delta T) + R_{L-}\Delta T, \end{aligned} \tag{77}$$

after rate limitation in %, ΔT is the time step over which the rate is limited, R_{L+} is the maximum increase rate of the lever setpoint and R_{L-} is the maximum decrease rate of the lever setpoint.

The relationship between the lever setpoint L_{set} and the propeller pitch and engine speed references P_{ref} and n_{ref} is expressed in the combinator curves for manoeuvring mode and transit mode, as illustrated in Fig. 8. The fuel injection limitations X_{lim} in % as a function of charge pressure p_1 in Pa and engine speed n_e in rev/s are represented in Tables 3 and 4.

The pitch is reduced when the fuel injection margin X_{mar} is below

Table 2
Unlimited lever setpoint L_u as a function of virtual shaft speed setpoint $n_{virt_{set}}$.

Virtual shaft speed	rpm	0	84	128	186	230
Unlimited lever setpoint	%	0	25	50	95	100

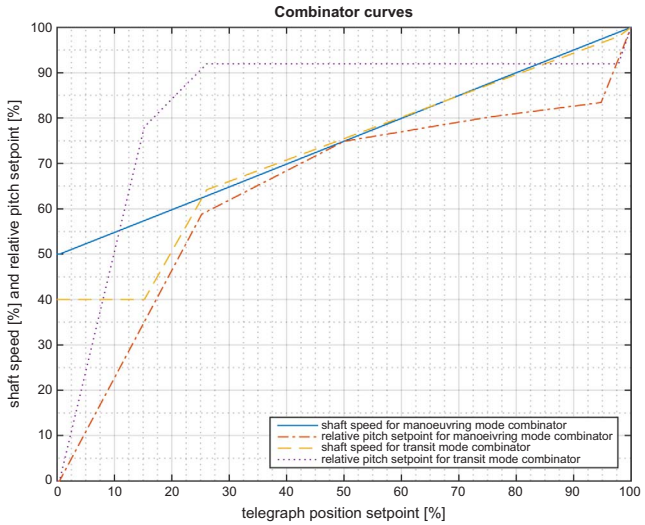

Fig. 8. Combinator curves for baseline control strategy in manoeuvring and transit modes.

Table 3
Fuel injection limitation X_{lim} as a function of charge pressure p_1.

Absolute charge pressure	kPa	0	100	300	350	400	500
Fuel injection limitation	%	42	42	103	109	115	115

Table 4
Fuel injection limitation X_{lim} as a function of engine speed n_e.

Engine speed	rpm	400	500	500	700	800	900	1000
Fuel limitation	%	40	46	55	67	84	105	105

$X_{mar_{min}}$ in order to prevent thermal overloading and the pitch increase rate R_{P+} is limited according to the linear relationship f_1 shown in Table 5, as follows:

$$X_{mar} = X_{lim} - X_{set} \tag{78}$$

$$X_{mar} < X_{mar_{min}}: R_{P+} = R_{Pr} \tag{79}$$

$$X_{mar} \geqslant X_{mar_{min}}: R_{P+} = f_1(n_{virt}) \tag{80}$$

where X_{set} is the fuel injection setpoint for the fuel pump in % and n_{virt} is the actual virtual shaft speed in rpm.

Subsequently, the pitch setpoint P_{set} is represented by the following equations:

$$P_{ref}(t) - P_{set}(t-\Delta T) > R_{P+}\Delta T: \quad P_{set}(t) = P_{set}(t-\Delta T) + R_{P+}\Delta T \tag{81}$$

$$R_{P-} \leqslant P_{ref}(t) - P_{set}(t-\Delta T) \leqslant R_{P+}: \quad P_{set}(t) = P_{ref}(t) \tag{82}$$

$$P_{ref}(t) - P_{set}(t-\Delta T) < R_{P-}\Delta T: \quad P_{set}(t) = P_{set}(t-\Delta T) + R_{P-}\Delta T, \tag{83}$$

where R_{P-} is the maximum decrease rate of the pitch setpoint.

The controller algorithm for the engine speed control that provides the fuel injection setpoint X_{set} is as follows:

$$X_{PID}(t) = K_P\left(\frac{n_{ref}(t)}{100} - \frac{n_e(t)}{n_{e_{nom}}}\right) + K_I \int_0^t \left(\frac{n_{ref}(t)}{100} - \frac{n_e(t)}{n_{e_{nom}}}\right) dt \tag{84}$$

$$X_{PID}(t) \leqslant X_{lim}(t): X_{set}(t) = X_{PID}(t) \tag{85}$$

$$X_{PID}(t) > X_{lim}(t): X_{set}(t) = X_{lim}(t), \tag{86}$$

where X_{PID} is the unlimited fuel injection setpoint, K_P is the proportional gain and K_I is the reset rate. The control parameters are listed in Table 6.

3.3. Control system tuning

The settings of the control parameters in Tables 2–6 and Fig. 8 have been determined through extensive dynamic simulations [71]. Because the relationship between the control parameters and the propulsion system MOEs is not very clear and depends on the operational conditions, the tuning requires weeks of analysing simulation time traces. Moreover, while the risk of thermal overloading has been eliminated, manoeuvrability, cavitation noise and fuel consumption might suffer from the conservative settings. However, the lack of MOPs to quantify system performance, has limited a thorough analysis of the trade-off between the various MOEs.

4. Validation of propulsion system model with conventional control

We use the terminology for model qualification, verification and validation as proposed in [76]. The model qualification, the analysis to obtain the conceptual model, and the conceptual model itself have been described in Section 2. We have performed the model verification per subsystem, as proposed in [17], for each of the subsystem models by varying the input parameters and comparing the response with analytical results (see Fig. 12 and 15).

Validation procedures with statistical analysis for a complex multidisciplinary simulation model have been described in [77–79,17,80]. [78] quantifies the uncertainty of the static model results by estimating the parameter uncertainty and running the simulation model for the extremes of the 95% confidence interval for the full model. Alternatively, [77] proposes to estimate the parameter uncertainty and subsequently determine the sensitivity of the sub-model either mathematically with Taylor approximations or numerically with infinitesimally small disturbances. Subsequently, the total ship model uncertainty can be established with linearisation by first order Taylor approximations. [79] compares these two methods with a case study and concludes the method proposed in [77] is more efficient while delivering comparable results. Subsequently, the validity of the model can be determined by comparing the model result interval with the confidence interval of measurements [78]. Another widely used method, Monte Carlo simulation, has been applied to a propulsion system model in [80]. While this method can handle non-linearities, as opposed to the method in [77], it does not provide insight in system behaviour. The main drawback of all these approaches is that the outcome of the statistical analysis strongly depends on the estimated parameter uncertainty and that other types of uncertainty are not addressed.

In our case, we want to establish how well we can predict the behaviour of a propulsion plant in uncertain operational conditions based on the model and its calibration with Factory Acceptance Test (FAT) data and determine how we can use this model to quantify the performance of the system and its control strategy for various MOEs. Subsequently, we want to use it to analyse the influence of the control strategy on the performance of the system as a whole quantified through a number of MOPs. Therefore, in this study we carry out quantitive validation with measurements of the ship in real operational conditions during the ships SAT.

Table 5
Pitch increase rate R_{P+} as a linear interpolation function f_1 of virtual shaft speed n_{virt}.

Virtual shaft speed	rpm	0	40	77	153	190	230	240
Pitch increase rate	%/s	3	2	1	1	0.5	0.2	0.2

Table 6
Control parameters in manoeuvring mode (MAN) and transit mode (TRAN)

Propulsion mode	MAN	TRAN
Proportional gain K_P	2	2
Reset rate K_I	0.5	0.5
Maximum lever increase rate R_{L+}	1.5%/s	3%/s
Maximum lever decrease rate R_{L-}	−3%/s	−6%/s
Pitch reduction rate R_{Pr}	−1.89%/s	−1.89%/s
Minimum injection margin $X_{mar_{min}}$	16.5%	16.5%
Maximum pitch reduction rate R_{P-}	−10%/s	−10%/s

4.1. Diesel engine model validation

The diesel engine models proposed in this study, or earlier versions proposed in [24,10], have not been validated in previous work. Therefore, this section first discusses the parametrisation and calibration of the model, based on the approach described in [17]. Subsequently, a quantitative validation wil be discussed using the full FAT data.

The parameters used in the diesel engine model have been obtained from four sources. Most engine parameters are available from the engine project guide and operating manual [81,12]. Furthermore, some parameters have been estimated based on diesel engine theory [50,48] or general physics theory. Finally, FAT results have given the remaining parameters, for calibration of the turbocharger efficiency as a function of the charge pressure, heat loss as a function of air flow and turbocharger entry temperature and heat release as a function of engine speed. The diesel engine parameters and their source have been summarised in Table 7.

The model is run at the FAT speed and power settings with the parameters from Table 7. The results in Figs. 9–11 show that the FAT measurements for specific fuel consumption, charge air pressure, combustion pressure, fuel injection and exhaust receiver temperature are within 5% of the model predictions. The turbocharger exit temperature is also reasonably predicted with the model, although the deviation at 25% load is slightly higher at 8%.

The FAT measurement data only consists of a limited amount of operating points in the full engine operating envelope, along the propeller curve. Full validation of the model requires measurements across all operating points of the engine. Therefore, a more extensive measurement campaign is recommended for further model validation. For completeness, Fig. 12 shows the specific fuel consumption and the air excess ratio over the complete operating envelope of the engine. When comparing this with the specific fuel consumption of a typical high speed engine in Fig. 14, as published in [11], the model results are within 5% down to 10% load of the engine. The minimum air excess ratio within the engine operating envelope is 1.4. This value can serve as a minimum air excess ratio that needs to be maintained in dynamic conditions. Fig. 13 shows the exhaust valve temperature and the exhaust receiver temperature, and therefore the entry temperature of the turbine. The trend of the exhaust valve temperature exactly matches the trend of the air access ratio, as previously demonstrated with modelling and experiments in [43]. This confirms that the air access ratio can serve as a good indicator for engine thermal loading. Although the trend of the exhaust receiver temperature shows an even bigger discontinuity at 900 rpm, the speed below which the cylinder bypass valve opens and provides extra cooling air to the exhaust receiver, the exhaust receiver temperature is also strongly influenced by the air access ratio.

4.2. Gearbox model validation

The gearbox loss model parameters a_{gb}, b_{gb} and c_{gb} and the nominal gearbox loss $P_{l_{nom}}$ in W were obtained from a linear fit through three data points of the gearbox manufacturer data and are presented in Table 8. When inspecting the results from the gearbox loss model in Fig. 15 and comparing them with the losses obtained from the manufacturers data over the full torque and speed envelop, we establish that the obtained values are within 1%, confirming the visual impression that the gearbox power losses exhibit a quadratic relationship with engine speed.

4.3. Propeller model validation

Available propeller models and data series have been discussed in [10] and an extensive review is available in [82]. In this study we use the Wageningen CD series, which represent 'contemporary and practical CPP designs' [60]. Moreover, the 5 blade propellers in this series represent CPP design 'aimed at applications for the navies' [60] and the design compromise was focused on 'better cavitation performance for high pitch and large blade area ratios ' [60]. We use the Wageningen C5-60 propeller, which has been made available to the partners in the Joint Industry Project on developing the Wageningen C- and D-series for Controllable Pitch Propellers (CPPs). This propeller has a similar open water diagram to the propeller fitted to the *Holland class* patrol vessel. The propeller parameters are presented in Table 9.

Because the Wageningen C5-60 propeller is not yet publicly available, this paper does not present the model results of this propeller

Table 7
Patrol vessel case study diesel engine model parameters from project guide (PG), physics theory (P), FAT data (F) or estimate (E).

Diesel engine parameter description	Value	Source
Nominal engine power $P_{e_{nom}}$	5400 kW	PG
Nominal engine speed $n_{e_{nom}}$	16.71 rev/s	PG
Number of cylinders i_e	12	PG
Number of revolutions per cycle k_e	2	PG
Bore diameter D_B	0.28 m	PG
Stroke length L_S	0.33 m	PG
Crank rod length L_{CR}	0.64063	PG
Crank angle after TDC, inlet closure α_{IC}	224 °	PG
Crank angle after TDC, exhaust open α_{EO}	119 °	PG
Nominal spec. fuel consumption $m_{bsfc_{nom}}$	198 g/kW h	PG
Heat release efficiency η_q	0.886	PG
Geometric compression ratio ε_c	13.8	PG
Total nominal mass flow $\dot{m}_{t_{nom}}$	10.5 kg/s	PG
Cylinder volume at state 1 V_1	0.0199 m^3	PG
Nominal pressure at state 1 $p_{1_{nom}}$	4.1e^5 Pa	PG
Maximum cylinder pressure $p_{max_{nom}}$	188e^5 Pa	PG
Temperature after the intercooler T_c	323 K	PG
Temperature of the inlet duct T_{inl}	423 K	E
Parasitic heat exchanger effectiveness ε_{inl}	0.05	E
Fuel injection time delay τ_X	0.0151 s	E
Turbocharger time constant τ_{TC}	51 s	E
Exhaust receiver time constant τ_{Pd}	0.01 s	E
Gas constant of air R_a	287 J/kg K	P
Specific heat at constant volume of air $c_{v,a}$	717.5 J/kg K	P
Specific heat at const. pressure of air $c_{p,a}$	1005 J/kg K	P
Specific heat at const. p of exhaust gas $c_{p,g}$	1100 J/kg K	P
Isentropic index of air κ_a	1.4	P
Isentropic index of the exhaust gas κ_g	1.353	P
Lower heating value of fuel h^L	42700 J/kg	PG
Stoichiometric air to fuel ratio σ_f	14.5	PG
Polytropic exponent for expansion n_{exp}	1.38	E
Polytropic exponent for blowdown n_{bld}	1.38	E
Nominal mechanical efficiency $\eta_{m_{nom}}$	0.90	E
Constant volume portion gradient $X_{cv_{grad}}$	−0.4164	F
Constant temperature portion $X_{ct_{nom}}$	0.4	E
Turbocharger factor a_η	−3.29e^{-12}	F
Turbocharger factor b_η	−2.52e^{-6}	F
Turbocharger factor c_η	0.2143	F
Ambient pressure p_{amb}	1e^5 Pa	PG
Ambient temperature T_{amb}	318 K	PG

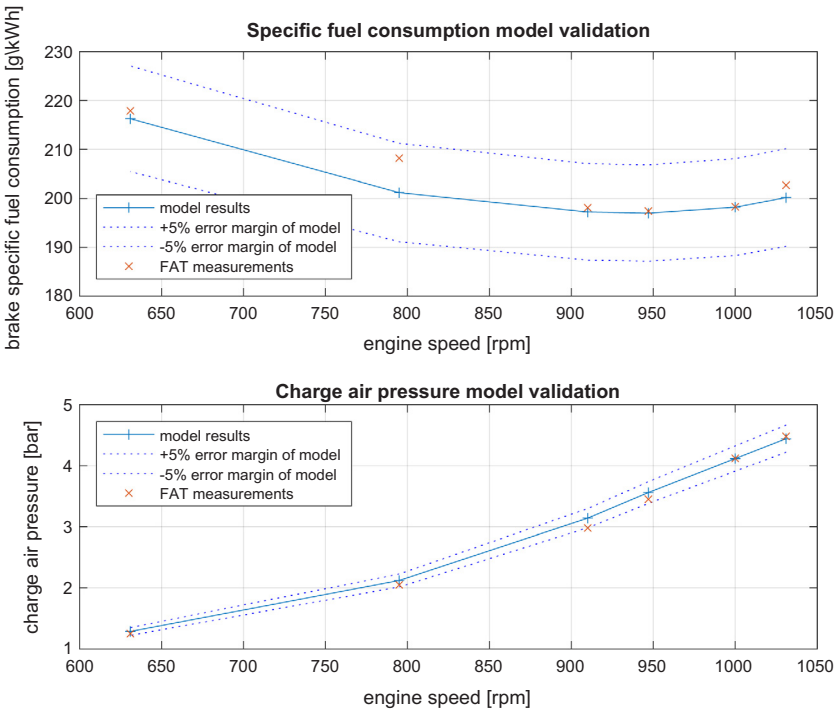

Fig. 9. Diesel engine model validation with FAT results for specific fuel consumption and charge air pressure.

separately. Clearly, the model uses the results of the open water tests, which is a well accepted method to model propeller thrust and torque within the assumptions of a homogenous advance speed, perpendicular flow into the propeller and quasi static performance. However, the modelling strategy and software code needs to be verified. For verification purposes we refer to the results of the C4-40 propeller presented in [10], which can be compared with the results presented in [19]. Moreover, for an uncertainty analysis of the method used to determine the Wageningen C- and D-series propellers, we refer to [60].

4.4. Hull and wave model validation

The ship resistance and the wave model parameters very strongly depend on the conditions in which the ship operates. In order to investigate the effect of varying conditions we consider three typical conditions. Trial condition is defined as Sea State 0, wind speed of 3 m/s and no fouling. Service condition is defined as Sea State 4, wind speed of 11 m/s, head seas and wind and 6 months out of dock fouling. Off-design condition is defined as Sea State 6, wind speed of 24 m/s, head seas and wind and 6 months out of dock fouling. The parameters that represent these conditions are shown in Table 10 and Fig. 16.

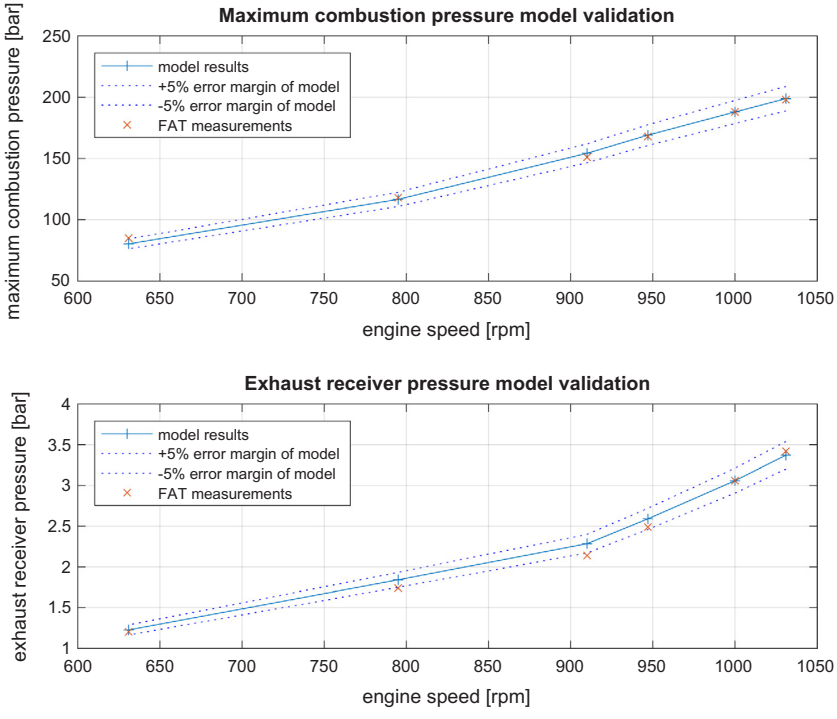

Fig. 10. Diesel engine model validation with FAT results for maximum combustion pressure and exhaust receiver pressure.

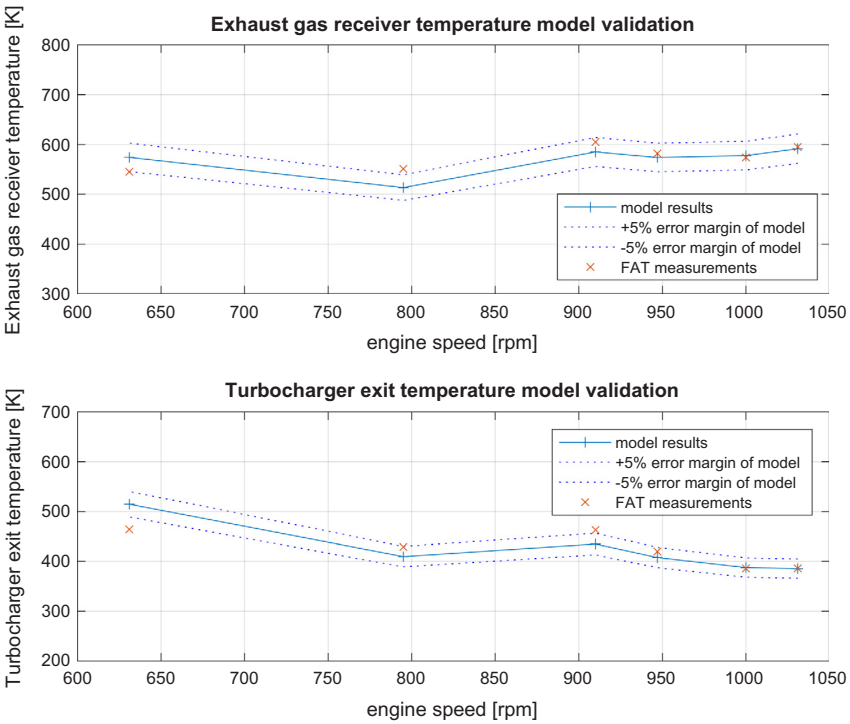

Fig. 11. Diesel engine model validation with FAT results for exhaust receiver and turbocharger exit temperature.

The validation of resistance test results is routinely performed by organisations such as MARIN, who have performed the resistance test. However, the total ship model validation demonstrates that the model's resulting ship speed corresponds with the tow tank test results. The verification of the behaviour of the propulsion plant in waves is performed with the total ship model based on ship measurements.

4.5. Total ship model validation

The total ship model consists of all the models discussed in Section 2 and of the control strategy described in Section 3.2. The parameters and validation of these models have been discussed in the previous Sections. The aim of this Section is to quantitatively validate the dynamic behaviour of the total ship model including the conventional control strategy. To this end, we compare the simulation results of an acceleration manoeuvre with the actual measurements of the same acceleration manoeuvre performed during the SAT's of *HNLMS Holland*, shown in Fig. 17. Even though the available measurements are limited, the available measurements deliver good confidence in the model credibility. Moreover, we compare the behaviour of the propulsion plant sailing at constant speed in waves with earlier measurements performed on a *Karel Doorman* class frigate in Sea State 6 as reported in [8].

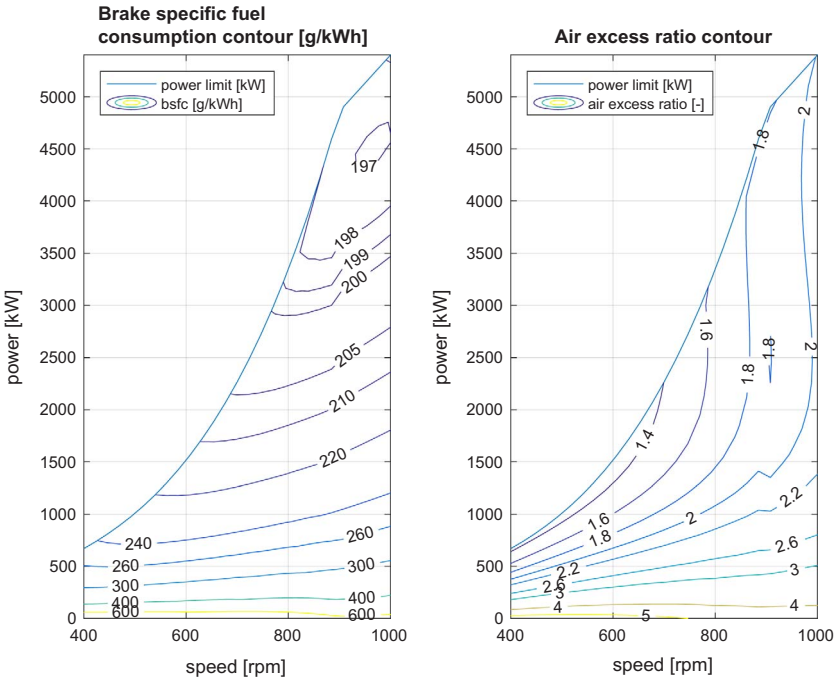

Fig. 12. Diesel engine model specific fuel consumption and air excess ratio results in complete operating envelope of the engine.

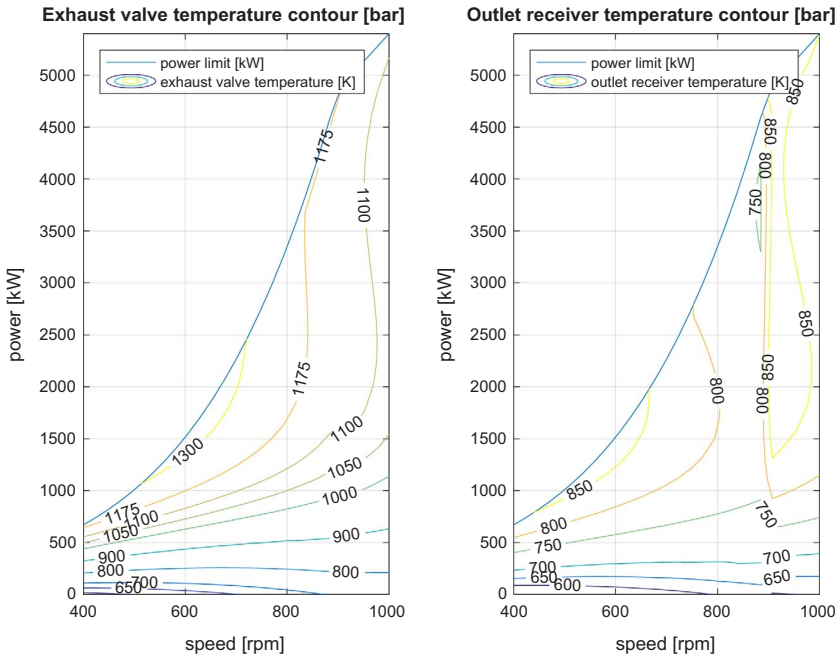

Fig. 13. Diesel engine model exhaust valve and exhaust receiver temperature results in complete operating envelope of the engine.

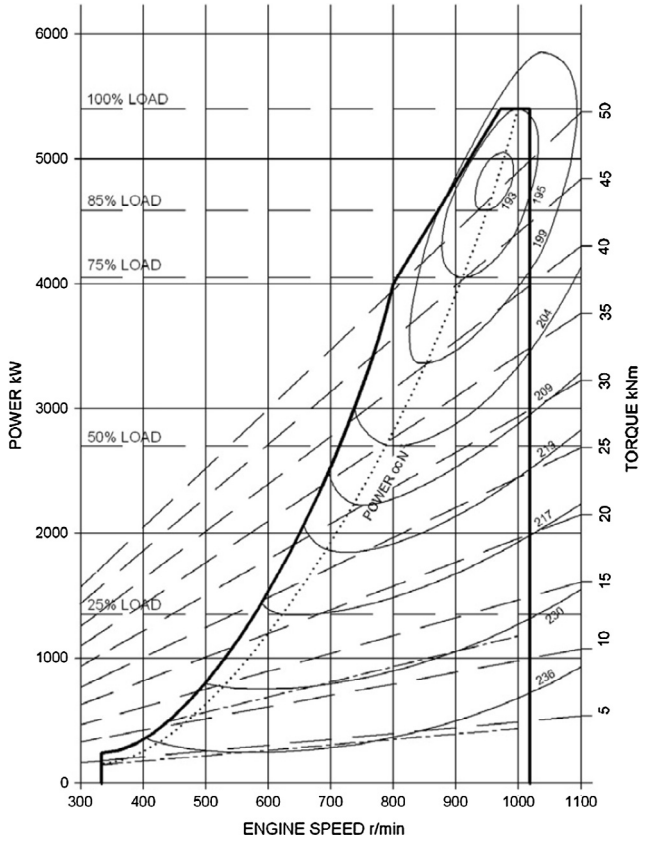

Fig. 14. Specific fuel consumption of typical high speed engine from [11].

4.5.1. Acceleration manoeuvre

The results of the acceleration manoeuvre from zero ship speed and a virtual shaft speed of 0 rpm to a setpoint of 230 rpm virtual shaft speed at time $t = 30$ s are presented in Figs. 18–20. The model results during the manoeuvre for fuel injection, shaft speed and virtual shaft speed stay within 5% of the measurements. The pitch has a larger deviation, but this is caused by the different open water diagram of the actual propeller compared to the C5-60 propeller that was used in the model.

Table 8
Gearbox parameters.

Gearbox loss parameter a_{gb}	0
Gearbox loss parameter b_{gb}	0.75
Gearbox loss parameter c_{gb}	0.25
Gearbox nominal power loss Pl_{nom} in kW	109
Gearbox speed reduction ratio i_{gb}	4.355
Nominal propeller speed $n_{p_{nom}}$ in rpm	230
Total inertia J_t in kg m^2	4600

The following main differences between the model results and the measurements can be identified:

- The model fuel pump position is approximately 2.5% higher than the measured fuel pump position at the start of the manoeuvre when the diesel engine load is below 10%. The results in Fig. 12 and 14 show the overestimated fuel consumption of the model causes this difference. This can possibly be resolved with more accurate modelling of the heat losses during expansion and blowdown after performing a more extensive measurement campaign on an engine, as discussed in Section 4.1.
- The response of the actual pitch has a time variant dead time of maximum 2 s on top of the linear delay. This delay is mainly caused by the counter balance valve as described in detail in [63]. [63] proposes to either remove the counter balance valve or maintain the control pressure of the counter balance valve if a fast pitch actuation is required to support an *angle of attack* control strategy as proposed in [7]. Then, a pitch actuation bandwidth of 0.6 Hz can be achieved. Alternatively, the nonlinear effects could be included in the model as proposed in [63,65,66] or the nonlinear effects could be neglected and the pitch actuation bandwidth of the model could be reduced to 0.15 Hz, leading to $\tau_P = 6.7$.
- The actual engine margin between $t = 105$ s and $t = 130$ s is significantly higher than the predicted engine margin. Because the charge pressure has not been logged the actual cause of this difference cannot be accurately determined. A possible cause is the nonlinear behaviour of the pitch actuation. However, the propeller pitch and engine loading of the model and the measurements in this time bracket do behave similarly. Therefore, the predicted performance of the total system model stays within 5% of the actual

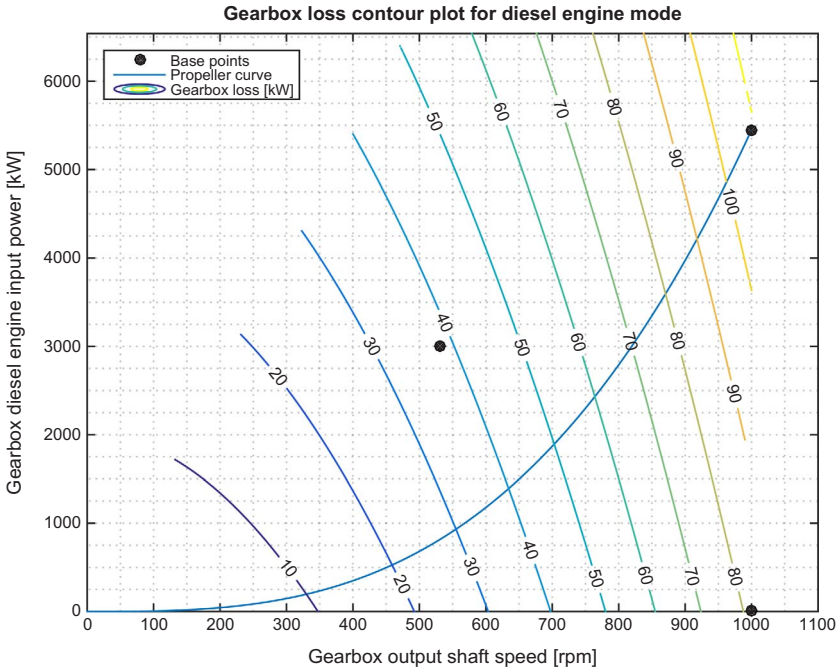

Fig. 15. Gearbox loss model contour plot with the three data points used for the linear fit and the propeller curve.

Table 9
Propeller parameters.

Wake fraction w	0.08
Relative rotative efficiency η_R	1
Propeller diameter D in m	3.2
Design pitch ratio at 0.7R P_d	0.8
Nominal pitch ratio at 0.7R P_{nom}	1.18
Pitch ratio for zero thrust P_0	0.068
First order pitch actuation delay τ_P	1.67
Vrijdag coefficient c_1	0.7
Shock free entry angle α_i	0

Table 10
Hull and wave model parameters in trial, design and off-design condition.

Condition	Trial	Service	Off-design
Ship mass m in 10^3kg		3800	
Number of propellers m		2	
Thrust deduction factor t		0.155	
Propeller centre depth z in m		6.5	
Wave amplitude ζ in m	0	1	2.5
Wave frequency ω in rad/s	–	0.966	0.628
Wave number k	–	0.095	0.0402

measurements.

- The combinator setpoint signal measured during the SAT exhibits what appears to be a high amount of signal noise. The signal is supposed to be constant at 93.5%, which is the final pitch setpoint associated with the virtual shaft speed of 230 rpm. Moreover, the signal features a spike at t = 30 s, before following the expected ramp. The cause of this noise is unknown but does not appear to influence the overall system response.

In summary, this quantitative validation demonstrates that the model predicts the total propulsion system behaviour within 5%.

4.5.2. Sailing in heavy seas

Measurements of sailing in heavy seas of the patrol vessel are not available. The only available measurements of a similar ship sailing in heavy seas have been reported in [17,8]. [8] report the measurements of a *Karel Doorman* class frigate in Sea State 6 and the results of these measurements are shown in Fig. 6.

To use these measurements for verification of the modelling strategy, we have changed the model parameters to reflect the main parameters of a typical frigate. The parameters used are shown in Table 11. For the hull and wave model parameters off-design conditions are assumed, as the reported results have been obtained in Sea State 6. Moreover, the pitch reduction strategy was not used in this simulation, because during the measurements no pitch reduction strategy was included in the control strategy and overloading actually occurred. Fig. 21 shows the results at 100 rpm virtual shaft speed of the propulsion system model that is modified to reflect a *Karel Doorman* class frigate.

The results in Fig. 21 demonstrate that the average magnitude of the disturbance of the engine speed and fuel injection due to the waves is predicted well: the fuel rack position fluctuates between 15 and 22 mm, with a nominal fuel rack position of 30 mm. The irregular effects of waves that clearly appear in the measurements in Fig. 6, are neglected in the model. Therefore, the propulsion system model does not predict the extreme values of the disturbance due to waves, but predicts the effect due to the significant wave height [73].

An accurate statistical analysis of the uncertainty of the model cannot be performed with these measurements, because the sea state only roughly determines the range of the wave height. For example, Sea State 6 is defined as a significant wave height between 4 and 6 m. More accurate loggings or measurements of the actual wave height would be required as input data for an accurate statistical analysis.

5. Measures of performance

Various standardised operating profiles have been determined in the automotive field to evaluate and compare MOPs of energy management strategies for hybrid electric vehicles, such as the world-harmonised light-duty vehicle test cycle (WLTC) and the new European driving cycle (NEDC) [83]. Moreover, a control benchmark simulation model exists for these control strategies [84]. These standards have not yet been defined for the evaluation of ship control strategies. Altosole et al. [85,86] propose the *slam start* and *crash stop* manoeuvres to evaluate control strategy performance during the most extreme acceleration and deceleration manoeuvres. While these manoeuvres are very valid to

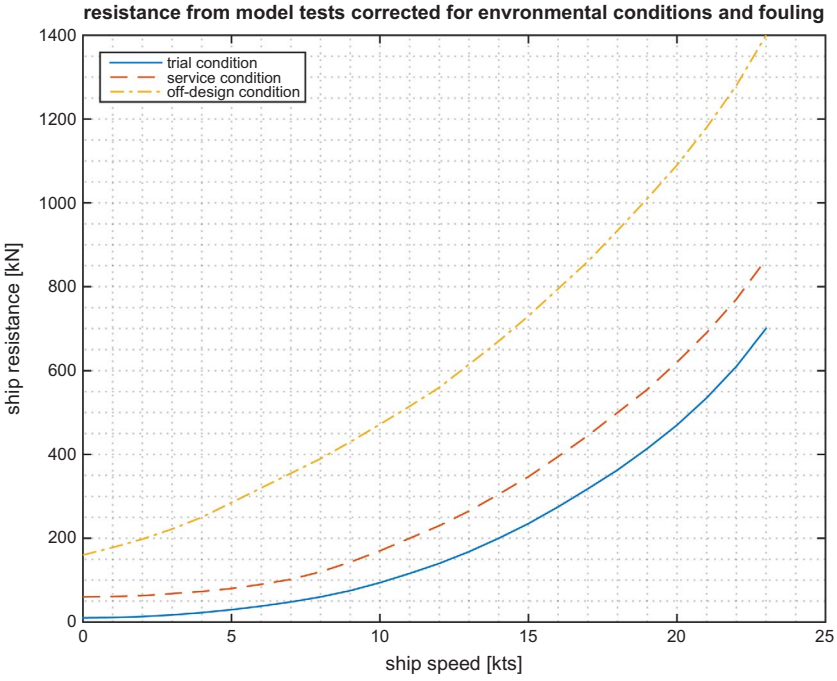

Fig. 16. Ship resistance from model tests corrected for environmental conditions and fouling in trial, service and off-design condition.

Fig. 17. *Zr. Ms. Holland.*

evaluate the feasibility of control strategies, they do not quantify MOEs, such as fuel consumption and engine loading, during regular operational conditions. [87] maps performance and emission parameters of a ship propulsion system in the engine operating envelope, but do not extend the analysis to measure ships effectiveness, for example expressing fuel consumption in ton/mile.

The aim of this paper is to evaluate MOEs fuel consumption, rate of acceleration, engine thermal loading and propeller cavitation with a validated model and obtain insight into the influence of the control strategy on holistic system performance. For this purpose, we propose the following benchmark manoeuvres: sail at constant speed in trial, design and off-design conditions and accelerate from 0 to 5, 5 to 10, 10 to 15 and 0 to 15 kts in design conditions. The acceleration from 0 to 15 kts is performed with the slam start manoeuvre: increasing the lever setpoint to maximum virtual shaft speed at once [65]. The other acceleration manoeuvres are performed by increasing the virtual shaft speed from the setting corresponding to the initial ship speed to the setting corresponding to the final ship speed. Moreover, we propose the following MOPs, obtained from these benchmark manoeuvres:

- Fuel consumption per mile for trial, design and off-design conditions, presented as a function of ships speed during sailing at constant speed, as previously proposed in [61, Ch12, pp. 482–483];
- Acceleration time for speed increases from 0 to 5, 5 to 10, 10 to 15 and 0 to 15 kts in design conditions;
- Average air excess ratio at constant speed for trial, design and off-design conditions, presented as a function of ship speed. This performance criterion serves as an indicator for engine thermal loading during constant speed sailing due to the average temperature;
- Minimum air excess ratio during speed increases from 0 to 5, 5 to 10, 10 to 15 and 0 to 15 kts in design conditions. This performance criterion serves as an indicator for engine thermal loading due to acceleration manoeuvres;
- Air excess ratio fluctuation at constant speed for design and off-design conditions, presented as a function of ship speed. This performance criterion serves as an indicator for thermal stresses in the engine caused by waves due to temperature fluctuation;
- Cavitation plot of acceleration manoeuvres from 0 to 5 and 5 to 10 kts in design conditions.

The MOPs of the baseline propulsion model and control system are shown in Figs. 22–26, Tables 12 and 13. These simulation results have been obtained with MATLAB Simulink R2016b software on a PC with Intel Core i7 processor and 16 GB memory. The required time to run all simulations to obtain these MOPs is 1 h.

5.1. Discussion

We can now compare the performance of the transit mode, with a combinator curve with relatively high pitch, low engine speed and slow acceleration rates for pitch and engine speed, with the performance of the manoeuvring mode, with a combinator curve with relatively low pitch, high engine speed and fast acceleration rates for pitch and engine speed and observe the following:

- The combinator curve of the transit mode achieves 30% less fuel consumption at 5 kts, 10% less fuel consumption at 10 kts and 2% less fuel consumption at 15 kts compared to the manoeuvring mode. The increased fuel consumption of the manoeuvring mode is mainly caused by the reduced open water efficiency of the propeller due to the reduced pitch. Further reducing fuel consumption can possibly

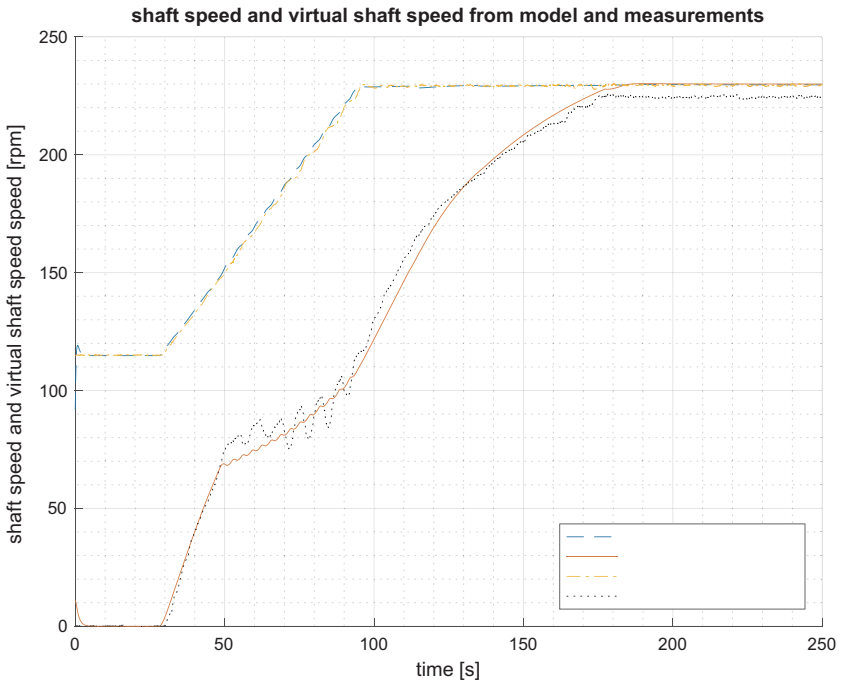

Fig. 18. Total ship model validation with SAT results for shaft speed and virtual shaft speed.

be achieved by further increasing the pitch during transit mode when the engine loading allows this, in trail and design conditions. In off-design conditions, however, the difference in fuel consumption disappears, because the pitch reduction enforces the same reduced pitch for the transit mode to prevent overloading of the engine.

- The air excess ratio at constant speed in manoeuvring mode is 0.1–0.3 higher than in transit mode, at low speeds when the pitch reduction mechanism is not limiting pitch. This lower air excess ratio leads to a significantly lower thermal loading of the engine, of approximately 30–90 K. This is caused by the lower pitch and higher engine revolutions and enables using higher acceleration rates for pitch and engine speed without thermally overloading the engine. Due to these high acceleration rates the acceleration time of the ship is in average 2 times faster in manoeuvring mode than in transit mode.
- In order to investigate the methodology of using the cavitation plot to assess the cavitation performance, we define a fictive cavitation bucket that matches the propeller and is centred at an angle of attack of 8 degrees. However, the shown cavitation buckets for these propeller have not been determined through measurement and are only shown to give some indication of the control strategy influence on cavitation behaviour. With this fictive cavitation bucket, the combinator curve of the transit mode falls within this bucket up to a speed of 10 kts for static conditions and only slightly violates the cavitation bucket during acceleration manoeuvres up tot the same

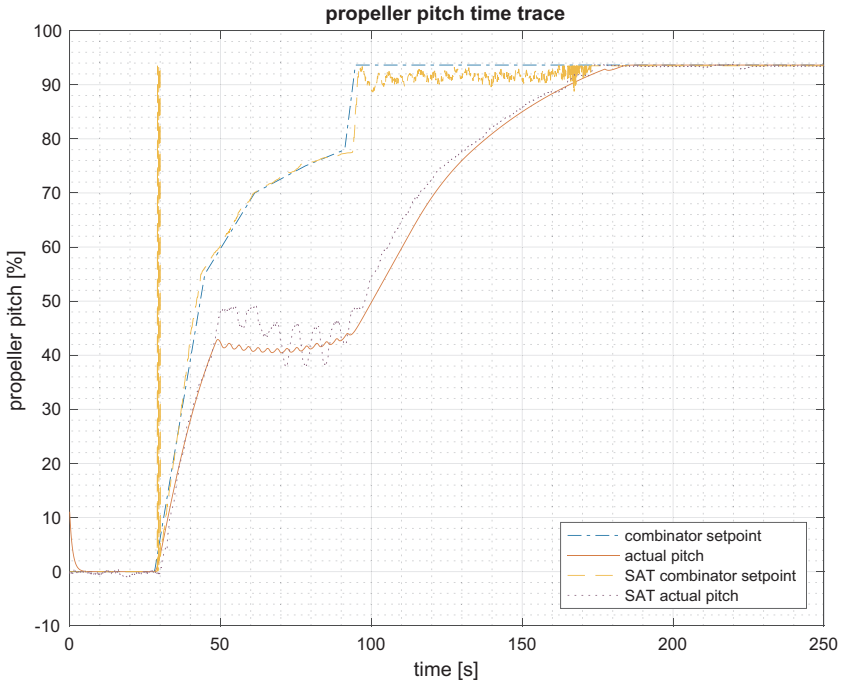

Fig. 19. Total ship model validation with SAT results for engine loading and margin.

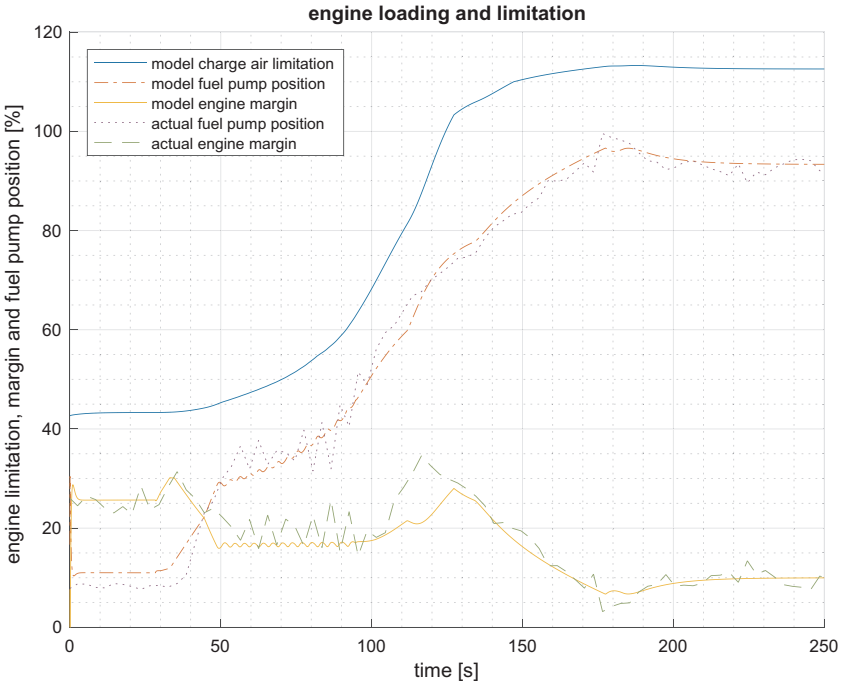

Fig. 20. Total ship model validation with SAT results for propellor pitch and propeller pitch setpoints.

Table 11
Changed propulsion model parameters to simulate a typical frigate, similar to *Karel Doorman* class at 100 rpm virtual shaft speed.

Parameter	value
Propeller diameter in m	4.2
Propeller pitch ratio at 100 rpm	1.2
Gearbox ratio	7.3

speed. Alternatively, the low pitch of the manoeuvring mode causes it to significantly violate the cavitation bucket. The cavitation plots for constant speed sailing and acceleration manoeuvres are both positioned outside the typical cavitation bucket.

In conclusion, the MOPs can be used to quickly and quantitatively asses the performance of a control strategy and its parameters. Moreover, these benchmark manoeuvres and performance criteria can be used to compare performance of alternative control strategies, but also of alternative propulsion configurations.

6. Conclusions and future research

A method is required to objectively and quickly quantify and assess the effectiveness of the system architecture and control strategy for diesel mechanical and hybrid propulsion systems. We have proposed a new diesel propulsion system model that can be parameterised with available manufacturer data. This model is based on a previous Mean Value First Principle (MVFP) model and has been improved to reflect

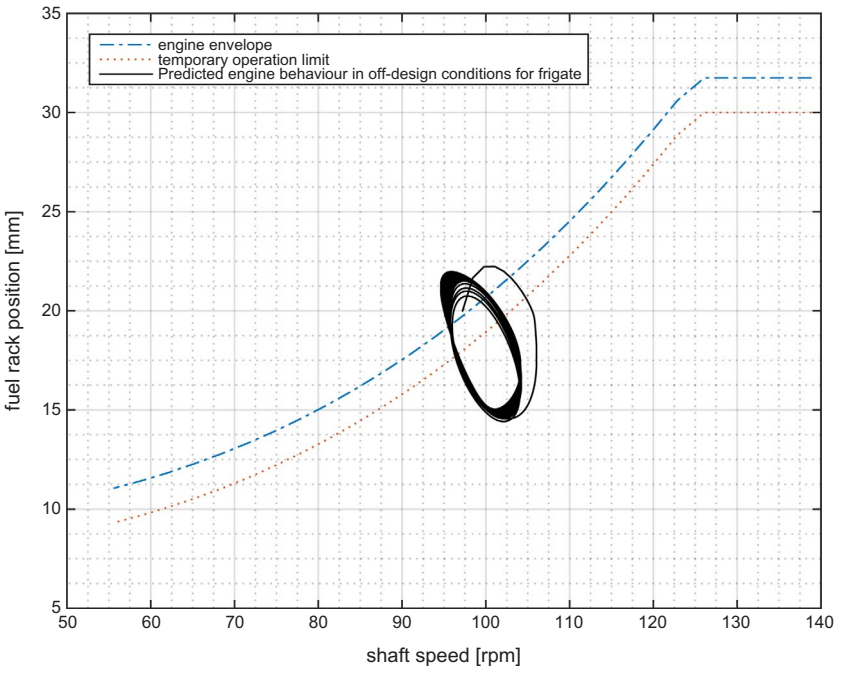

Fig. 21. Total ship model validation of simulated M-frigate at 100 rpm in Sea State 6.

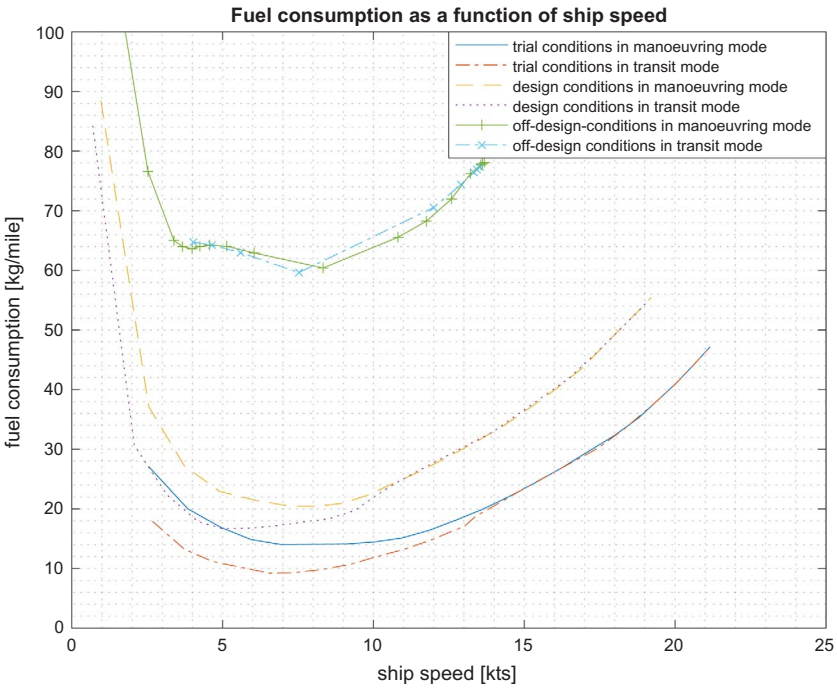

Fig. 22. Fuel consumption plot as a function of ships speed for various conditions in manoeuvring and transit mode.

modern turbocharger and Miller-timing behaviour based on advanced diesel engine theory. Subsequently, we have validated the MVFP diesel engine model with measurements in factory conditions and in operational conditions at sea with a case study naval vessel. The predictions of the diesel engine model were within 5% of most measurement values. Although exhaust gas temperatures were only predicted within 10% of the measurements, the engine thermal loading can be accurately quantified with the air excess ratio.

The baseline control strategy with fixed combinator curves, acceleration limitations and pitch reduction strategy has been described. We have shown that this strategy can prevent engine overloading effectively while achieving conservative manoeuvrability, acceleration and cavitation behaviour. Quantitative validation has demonstrated that the propulsion system model credibly predicts propulsion system behaviour within 5% accuracy. Moreover, the wave model behaviour in Sea State 6 has been verified with the propulsion system model with modified parameters that reflect a frigate. The results of this model were found to match measurements on a frigate in Sea State 6.

Finally, the paper proposes benchmark manoeuvres and associated measures of performance (MOPs) to quantify the performance of the

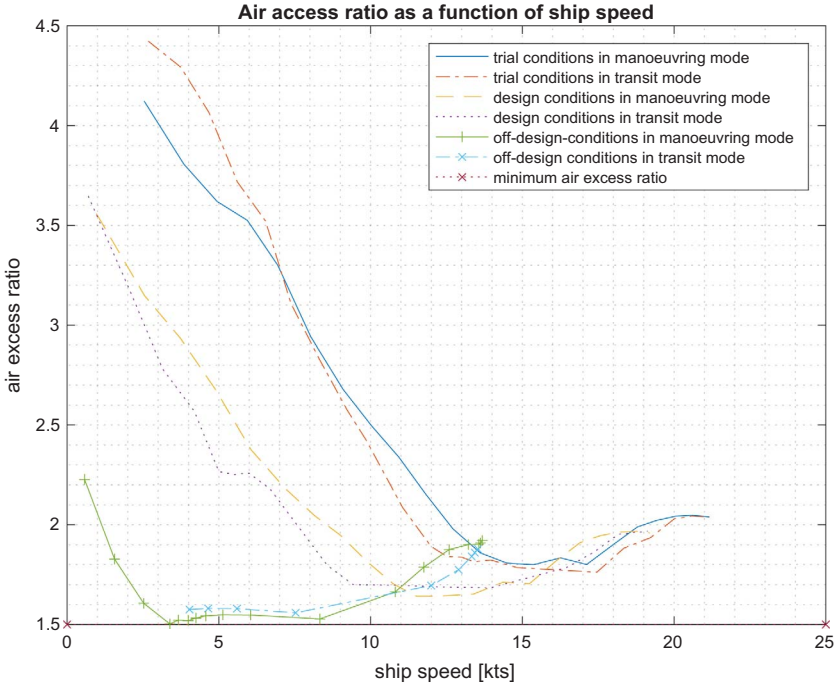

Fig. 23. Air excess ratio plot as a function of ships speed for various condition in manoeuvring and transit mode.

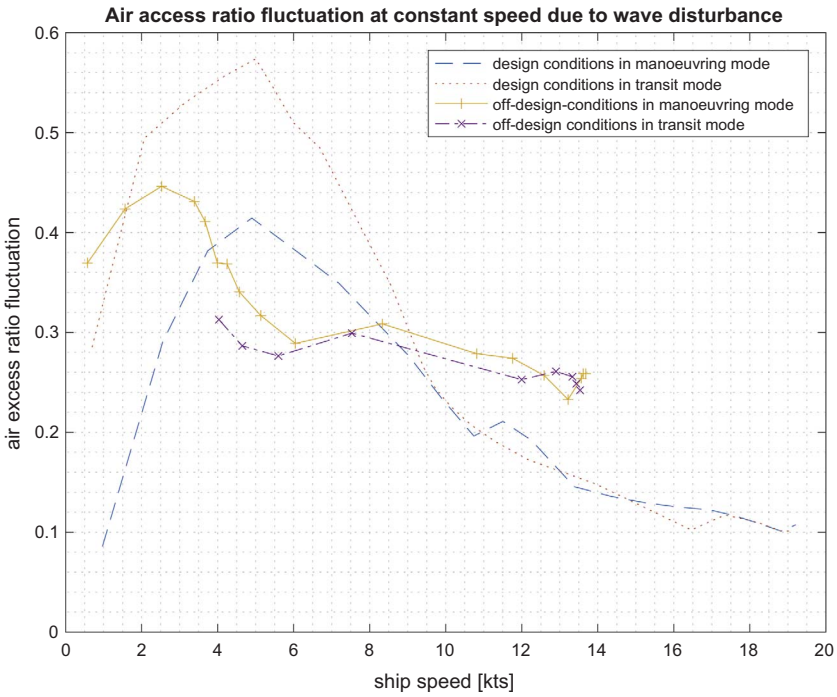

Fig. 24. Air excess ratio fluctuation plot as a function of ships speed for design and off-design conditions in manoeuvring and transit mode.

propulsion plant on the following measures of effectiveness (MOEs): fuel consumption, rate of acceleration, engine thermal loading and propeller cavitation. These MOPs and the propulsion system model have been used to evaluate the performance of two operating modes of the conventional control strategy. Analysing these two control modes previously either required days of sea trials, or weeks of analysing various simulation time traces. Alternatively, the proposed MOPs can be determined within an hour of simulation time. Depending on the particular control strategy and operating conditions, fuel savings up to 30%, thermal loading reduction of 90 K and reductions of 50% in acceleration time can be achieved.

Future work will use the model proposed in this paper to evaluate an adaptive pitch control strategy that aims to reduce fuel consumption and emissions, improve the ships manoeuvrability and reduce cavitation noise while preventing engine overloading. Adding an induction motor model, as proposed in [88] will allow to evaluate the performance of hybrid propulsion plants with CPP as well.

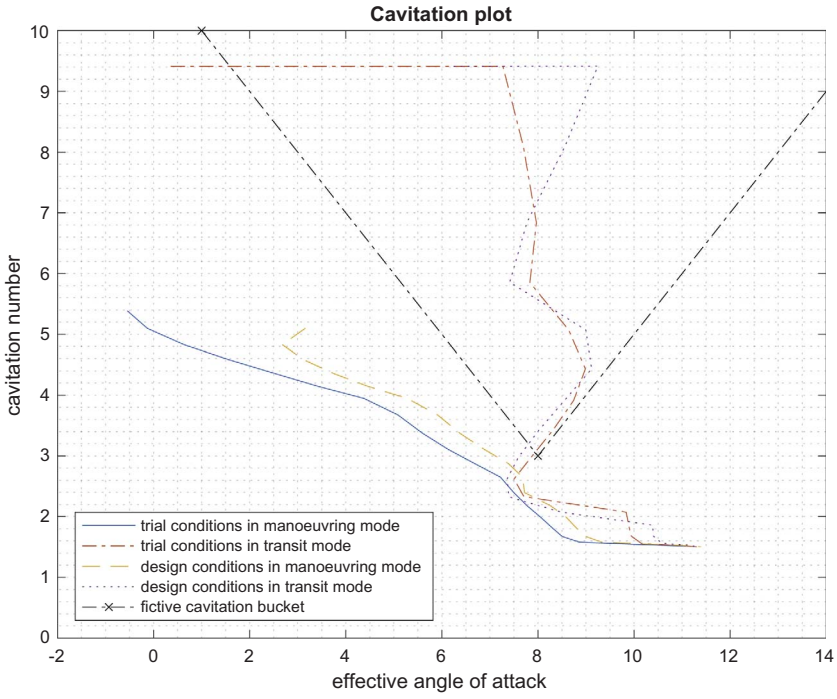

Fig. 25. Cavitation plot from low speed to maximum speed for various conditions in manoeuvring and transit mode.

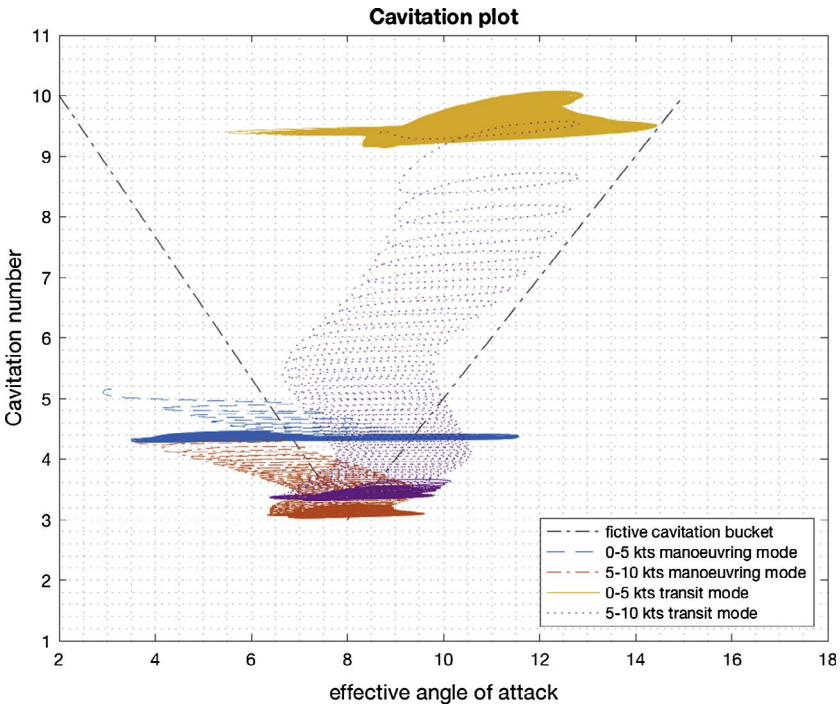

Fig. 26. Cavitation plot for acceleration manoeuvres at design condition in manoeuvring and transit mode.

Table 12
Acceleration time, minimum air excess ratio and maximum angle of attack during acceleration in manoeuvring mode (design condition).

Criterion	0–5 kts	5–10 kts	5–15 kts	0–15 kts
Acceleration time (s)	100	114	80	100
Air excess ratio	1.77	1.65	1.65	1.75
Angle of attack (deg)	9.6	10.6	12.6	12.2

Table 13
Acceleration time, minimum air excess ratio and maximum angle of attack during acceleration in transit mode (design condition).

Criterion	0–5 kts	5–10 kts	5–15 kts	0–15 kts
Acceleration time (s)	384	845	152	170
Air excess ratio	1.67	1.63	1.64	1.76
Angle of attack (deg)	12.8	11.1	12.4	10.7

Acknowledgement

This project is partially supported by project 'ShipDrive: A Novel Methodology for Integrated Modelling, Control, and Optimization of Hybrid Ship Systems' (project 13276) of Dutch Technology Foundation STW and by the Royal Netherlands Navy. The Royal Netherlands Navy supplied Fig. 17. Fig. 6, ©IFAC 2001, was reproduced from [8] with permission.

Special thanks goes to Maarten de Boer and Ilham Hardy of Shipdrive Partner Damen Schelde Naval Shipbuilding for preparing and providing the validation data in FAT and SAT measurements and to dr. Arthur Vrijdag and prof. Douwe Stapersma for reviewing the manuscript and providing advice to improve the scientific quality and readability of this article.

Appendix A. Supplementary material

Supplementary data associated with this article can be found, in the online version, at http://dx.doi.org/10.1016/j.apenergy.2017.09.103.

References

[1] IMO. Third IMO greenhouse gas study 2014, exec. summary and final report. Tech. rep., IMO, London, UK; 2015.
[2] Roskilly AP, Palacin R, Yan J. Novel technologies and strategies for clean transport systems. Appl Energy 2015;157:563–6. http://dx.doi.org/10.1016/j.apenergy.2015.09.051.
[3] van Oers B. A packing approach for the early stage design of service vessels [Ph.D. thesis]. The Netherlands: Faculty 3ME, Delft U of T; 2011.
[4] Roedler GJ, Jones C. Technical measurement, a coll. project of PSM, INCOSE and industry. v 1.0 INCOSE-TP-2003-020-01. INCOSE; 2005.
[5] Grimmelius HT, Stapersma D. Control optimisation and load prediction for marine diesel engines using a mean value first principle model. In: Proc MS & TES, Newcastle-upon-Tyne, UK; 2000. p. 212–9.
[6] Grimmelius HT, Stapersma D. The impact of propulsion plant control on diesel engine thermal loading. In: Proc 22nd CIMAC WC, Hamburg, Germany; 2001.
[7] Vrijdag A, Stapersma D, van Terwisga T. Control of propeller cavitation in operational conditions. J Mar Eng Technol 2010;16:15–26.
[8] Van Spronsen P, Toussain R. An optimal control approach to preventing marine diesel engine overloading aboard Karel Doorman class frigates. In: Proc. IFAC CAMS, Glasgow, UK; 2001. p. 23–30.
[9] Geertsma RD, Negenborn RR, Visser K, Hopman JJ. Design and control of hybrid power and propulsion systems for smart ships: a review of developments. Appl Energy 2017;194:30–54. http://dx.doi.org/10.1016/j.apenergy.2017.02.060.
[10] Geertsma RD, Negenborn RR. Visser K, Hopman JJ. Torque control for diesel mechanical and hybrid propulsion for naval vessels. In: Proc. 13th INEC, Bristol, UK; 2016. p. 476–92.
[11] van Straaten OFA, de Boer MJ. Optimum propulsion engine configuration from fuel economic point of view. In: Proc 11th INEC, Edinburgh, UK; 2012.
[12] MAN Diesel SE. Project guide for marine plants diesel engine 28/33d prelim. Tech. rep. MAN Diesel SE, Augsburg, Germany; May 2008.
[13] Guan C, Theotokatos G, Zhou P, Chen H. Computational investigation of large containership propulsion engine operation at slow steaming conditions. Appl Energy 2014;130:370–83. http://dx.doi.org/10.1016/j.apenergy.2014.05.063.
[14] Kyrtatos NP, Koumbarelis I. Performance prediction of next generation slow speed diesel engines during ship manoeuvres. Trans IMarE 1994;106(Part 1):1–26.
[15] Schulten P. The interaction between diesel engines, ship and propellers during manoeuvring [PhD thesis]. Faculty 3ME, Delft U of T; 2005.
[16] Martelli M. Marine propulsion simulation. Warsaw/Berlin: De Gruyter Open Ltd; 2014.
[17] Vrijdag A. Control of propeller cavitation in operational conditions [PhD thesis]. The Netherlands: Faculty 3ME, Delft U of T; 2009.
[18] Deleroi KHE. Simulation study of acceleration and crash stop manoeuvres for ship machinery systems [MSc. thesis]. the Netherlands: Faculty 3ME, Delft U of T; 1995.
[19] Dang J, van den Boom H., Ligtelijn JT. The Wageningen C- and D-series propellers. In: Proc. 12th FAST, Amsterdam, the Netherlands; 2013.
[20] Kuiper G. The Wageningen propeller series, publication 92-001, MARIN; 1992.
[21] Hendricks E. Engine modelling for control applications: a critical survey. Meccanica 1997;32:387–96.
[22] Grimmelius HT, Mesbahi E, Schulten PJM, Stapersma D. The use of diesel engine simulation models in ship propulsion plant design and operation. In: 25th CIMAC WC, Vienna, Austria; 2007.

[23] Ding Y, Stapersma D, Grimmelius H. Using parametrized finite combustion stage models to characterize combustion in diesel engines. Energy Fuels 2012;26:7099–106. http://dx.doi.org/10.1021/ef3014212.

[24] Miedema SA, Lu Z. The dynamic behaviour of a diesel engine. In: Proc WEDA XXII TC, Denver, Colorado, USA; 2002.

[25] Miller RH. Supercharging and internal cooling for high output. ASME Trans 1947;69:453–7.

[26] Wang Y, Lin L, Zeng S, Huang J, Roskilly AP, He Y, et al. Application of the miller cycle to reduce NOx emissions from petrol engines. Appl Energy 2008;85:463–74. http://dx.doi.org/10.1016/j.apenergy.2007.10.009.

[27] Colonna P, van Putten H. Dynamic modelling of steam power cycles. Part I – modelling paradigm and validation. Appl Therm Eng 2007;27:467–80. http://dx.doi.org/10.1016/j.applthermaleng.2006.06.011.

[28] Shi W, Grimmelius HT, Stapersma D. Analysis of ship propulsion system behaviour and the impact on fuel consumption. Int Shipbuild Progr 2010;57:35–64.

[29] Schulten PJM, Stapersma D. Mean value modelling of the gas exchange of a 4-stroke diesel engine for use in powertrain applications. In: SAE technical papers; 2003. http://dx.doi.org/10.4271/2003-01-0219.

[30] Nielsen KV, Blanke M, Eriksson L. Control-oriented model of molar scavenge oxygen fraction for exhaust recirculation in large diesel engines. Meas Contr 2017;139:02100701–10.

[31] Nielsen KV, Blanke M, Eriksson L, Vejlgaard-Laursen M. Adaptive feedforward control of exhaust gas recirculation in large diesel engines. Contr Eng Pract 2017;65:26–35. http://dx.doi.org/10.1016/j.conengprac.2017.05.003.

[32] Ding Y. Characterising combustion in diesel engines [PhD thesis]. The Netherlands: Faculty 3ME, Delft U of T; 2011.

[33] Jensen JP, Kristensen AF, Sorenson SC, Houbak N, Hendricks E. Mean value modelling of a small turbocharged diesel engine. In: SAE technical papers; 1991. http://dx.doi.org/10.4271/910070.

[34] Ghojel JI. Review of the development and applications of the Wiebe functions: a tribute to the contribution of Ivan Wiebe to engine research. Int J Engine Res 2010;11:297–312.

[35] Baldi F, Theotokatos G, Andersson K. Development of a combined mean value-zero dimensional model and application for a large marine four-stroke diesel engine simulation. Appl Energy 2015;154:402–15. http://dx.doi.org/10.1016/j.apenergy.2015.05.024.

[36] Benvenuto G, Campora U. Dynamic simulation of a high-performance sequentially turbocharged marine diesel engine. Int J Engine Res 2002;3(3):115–25.

[37] Scappin F, Stefansson SH, Haglind F, Andreasen A, Larsen U. Validation of a zero-dimensional model for prediction of NOx and engine performance for electronically controlled marine two-stroke diesel engines. Appl Therm Eng 2012;37:344–52. http://dx.doi.org/10.1016/j.applthermaleng.2011.11.047.

[38] Raptosasios S, Sakellaridis NF, Papagiannakis RG, Hountalas DT. Application of a multi-zone combustion model to investigate the NOx reduction potential of two-stroke marine diesel engines using EGR. Appl Energy 2015;157:814–23. http://dx.doi.org/10.1016/j.apenergy.2014.12.041.

[39] Zeldovich YB. The oxidation of nitrogen in combustion and explosions. Acta Phys URSS 1946;21(4):577–628.

[40] Millo F, Mallamo F, Pautasso E, Mego GG. The potential of electric exhaust gas turbocharging for HD diesel engines. In: SAE technical papers, Detroit, Michigan, USA; 2006. http://dx.doi.org/10.4271/2006-01-0437.

[41] Pasini G, Lutzemberger G, Frigo S, Marelli S, Ceraolo M, Gentili R, et al. Evaluation of an electric turbo compound system for SI engines: a numerical approach. Appl Energy 2016;162:527–40. http://dx.doi.org/10.1016/j.apenergy.2015.10.143.

[42] Pang KM, Karvounis N, Walther JH, Schramm J. Numerical investigation of soot formation and oxidation processes under large two-stroke marine diesel engine-like conditions using integrated CFD-chemical kinetics. Appl Energy 2016;169:874–87. http://dx.doi.org/10.1016/j.apenergy.2016.02.081.

[43] Sapra H, Godjevac M, Visser K, Stapersma D, Dijkstra C. Experimental and simulation-based investigations of marine diesel engine performance against static back-pressure. Appl Energy 2017;204:78–92. http://dx.doi.org/10.1016/j.apenergy.2017.06.111.

[44] Barsingerhorn JS, Limburg JS, de Man EC, Wieleman VA. Turbodrive [Bsc. thesis]. The Netherlands: Faculty 3ME, Delft U of T; 2015.

[45] Mestemaker BTW, Georgescu I. Diesel and dual fuel engine model, unpublished rep. Kinderdijk (The Netherlands): MTI Holland BV; 2014.

[46] Sui C, Song E, Stapersma D, Ding Y. Mean value modelling of diesel engine combustion based on parameterized finite stage cylinder process. Ocean Eng 2017;136:218–32. http://dx.doi.org/10.1016/j.oceaneng.2017.03.029.

[47] Dixon SL. Fluid mechanics and thermodynamics of thermomachinery. 4th ed. Heinemann: Butterworth; 1998.

[48] Stapersma D. Diesel engines – a fundamental approach to performance analysis, turbocharging, combustion, emissions and heat transfer. In: 8th Edition: turbocharging, Part I: diesel engines a – performance analysis and turbocharging, NLDA, vol. 2; 2010.

[49] Asad U, Zheng M. Exhaust gas recirculation for advanced diesel combustion cycles. Appl Energy 2014;123:242–52. http://dx.doi.org/10.1016/j.apenergy.2014.02.073.

[50] Stapersma D. Diesel engines – a fundamental approach to performance analysis, turbocharging, combustion, emissions and heat transfer. Performance analysis, part I: diesel engines a – performance analysis and turbocharging, NLDA, 8th ed., vol. 1; 2010.

[51] Stapersma D. Diesel engines – a fundamental approach to performance analysis, turbocharging, combustion, emissions and heat transfer. turbocharging, part I: diesel engines a – performance analysis and turbocharging, NLDA, 8th ed., vol. 2; 2010.

[52] Betz A, Woschni G. Energy conversion rate and rate of heat release of turbocharged diesel engines under transient conditions. MTZ Motortechnische Zeitschrift 1986;47(7–8):263–7.

[53] Zinner K. Aufladung von Verbrennungsmotoren. 2nd ed. Berlin, Heidelberg, New York: Springer-Verlag; 1980.

[54] Chen S, Flynn P. Development of a single cylinder compression ignition research engine. In: SAE technical paper of comb. powerpl. and transport. meet, Cleveland, Ohio, USA; 1965. http://dx.doi.org/10.4271/650733.

[55] Concli F, Gorla C. Numerical modelling of the power losses in geared transmissions: windage, churning and cavitation simulations with a new integrated approach that drastically reduces the computational effort. Tribol Int 2016;103:58–68. http://dx.doi.org/10.1016/j.triboint.2016.06.046.

[56] Godjevac M, Drijver J, de Vries L, Stapersma D. Evaluation of losses in maritime gearboxes. Proc IMechE, Part M: J Eng Marit Environ 2015:1–16.

[57] Stapersma D. The importance of (e)mission profile for naval ships. In: Proc 7th INEC, Plymouth, UK; 1994. p. 83–100.

[58] Taylor DW. The speed and power of ships: a manual of marine propulsion. Washington D.C. (USA): Press of Ransdell, Inc.; 1933.

[59] Gawn RWL. Effect of pitch and blade width on propeller performance. Trans RINA 1952:157–93.

[60] Dang J, Brouwer J, Bosman R, Pouw C. Quasi-steady two-quadrant open water tests for the Wageningen Propeller C- and D-series. In: Proc. 29th symp on naval hydrodynamics, Gothenburg, Sweden; 2012.

[61] Klein Woud H, Stapersma D. Design of propulsion and electric power generation systems. London, UK: IMarEST; 2012.

[62] Grimmelius HT, Bakker JC, Wesselink A. The use of non linear models in the analysis of CPP actuator behaviour. Marine engineering systems. London, UK: IMarEST; 2006. p. 240–54.

[63] Wesselink AF, Stapersma D, van den Bosch D. Non-linear aspects of propeller pitch control. In: Proc. 8th INEC, London, UK; 2006.

[64] Godjevac M, van Beek T, Grimmelius HT, Tinga T, Stapersma D. Prediction of fretting motion in a controllable pitch propeller during service. Proc IMechE Part M: J Eng Marit Environ 2009;223:541–60.

[65] M. Altosole, M. Marteli, S. Vignolo, A mathematical model of the propeller pitch change mechanism for the marine propulsion control design. In: Proc 14th intern. congress of the intern. maritime ass. of the med., Genova, Italy, vol. 2; 2012. p. 649–56.

[66] Martelli M, Figari M, Altosole M, Vignolo S. Controllable pitch propeller actuating mechanism, modelling and simulation. Proc IMechE Part M: J Eng Marit Environ 2014;228:29–43. http://dx.doi.org/10.1177/1475090212468254.

[67] van Terwisga T, vn Wijngaarden E, Bosschers J, Kuiper G. Achievements and challenges in cavitation research on ship propellers. International shipbuilding progress. IOS Press; 2007. p. 165–87.

[68] Gaggero S, Tani G, Viviani M, Conti F. A study on the numerical prediction of propellers cavitating tip vortex. Ocean Eng 2014;92:137–61. http://dx.doi.org/10.1016/j.oceaneng.2014.09.042.

[69] Martelli M, Viviani M, Altosole M, Figari M, Vignolo S. Numerical modelling of propulsion, control and ship motions in 6 degrees of freedom. Proc IMechE Part M: J Eng Marit Environ 2014;228(4):373–97. http://dx.doi.org/10.1177/1475090214544181.

[70] Holtrop J. A statistical re-analysis of resistance and propulsion data. Int Shipbuild Progr 1984;28(363):272–6.

[71] de Boer M, Hardy I. Final dynamic simulations PS. Tech. rep. E40800/E1200.58. Damen Schelde Naval Shipbuilding; 2011.

[72] Gerritsma J, Beukelman W. Analysis of the resistance increase in waves of a fast cargo ship. Int Shipbuild Progr 1972;19(217):285–93.

[73] Gerritsma J. Bewegingen en sturen 1 - Golven. MT513, report 473-K. Delft U of T: Faculty 3ME; 1989.

[74] Guillemette JR, Bussières P. Proposed optimal controller for the Canadian patrol frigate diesel propulsion system. In: Proc. 11th SCSS, Southampton, UK; 1997. p. 507–30.

[75] Xiros N. Robust control of diesel ship propulsion. London, UK: Springer-Verlag; 2002.

[76] Schlesinger S, Crosbie RE, Gagne RE, Innis GS, Lalwani CS, Loch J, et al. Terminology for model credibility. Simulation 1979:103–4.

[77] Du X, Chen W. Efficient uncertainty analysis methods for multidisciplinary robust design. AIAA J 2002;40:545–52.

[78] Schulten P, Stapersma D. A study of the validity of a complex simulation model. J Mar Eng Technol 2007;10.

[79] Vrijdag A, Schulten P, Stapersma D, van Terwisga T. Efficient uncertainty analysis of a complex multidisciplinary simulation model. J Mar Eng Technol 2007;10.

[80] Vrijdag A. Estimation of uncertainty in ship performance predictions. J Mar Eng Technol 2014;13:45–55.

[81] MAN Diesel SE. Operating and maintenance manual for marine plants diesel engine 28/33d. Technical report. MAN Diesel SE, Augsburg, Germany; May 2008.

[82] Carlton JS. Marine propulsion and propellers. 3rd ed. London, GB: Butterworth Heinemann; 2012.

[83] Ko J, Jin D, Jang W, Myung C-L, Kwon S, Park S. Comparative investigation of NOx emission characteristics from a euro 6-compliant diesel passenger car over the NEDC and WLTC at various ambient temperatures. Appl Energy 2017;187:652–62. http://dx.doi.org/10.1016/j.apenergy.2016.11.105.

[84] Sciarretta A, Serrao L, et al. A control benchmark on the energy management of a plug in hybrid electric vehicle. Contr Eng Pract 2014;29:287–98.

[85] Altosole M, Figari M, Martelli M, Orru G. Propulsion control optimisation for emergency manoeuvres of naval vessels. Proc 11th INEC. 2012.

[86] Altosole M, Martelli M. Propulsion control strategies for ship emergency manoeuvres. Ocean Eng 2017;137:99–109. http://dx.doi.org/10.1016/j.oceaneng.2017.03.053.

[87] Theotokatos G, Tzelepis V. A computational study on the performance and emission parameters mapping of a ship propulsion system. Proc IMechE Part M: J Eng Marit Environ 2015;229(1):58–76. http://dx.doi.org/10.1177/1475090213498715.

[88] Geertsma RD, Negenborn RR, Visser K, Hopman JJ. Parallel control for hybrid propulsion of multifunction ships. In: Conf. proc. 20th IFAC world congr., Toulouse, France; 2017.